

**Search for supersymmetry using boosted Higgs bosons and
missing transverse momentum in proton-proton collisions
at 13 TeV**

by

Frank Jensen

M.S., University of Colorado Boulder, 2014

B.A., University of California Berkeley, 2008

A thesis submitted to the
Faculty of the Graduate School of the
University of Colorado in partial fulfillment
of the requirements for the degree of
Doctor of Philosophy
Department of Physics

2018

This thesis entitled:
Search for supersymmetry using boosted Higgs bosons and missing transverse momentum in
proton-proton collisions at 13 TeV
written by Frank Jensen
has been approved for the Department of Physics

Professor Kevin Stenson

Professor William Ford

Professor Jamie Nagle

Professor Markus Pflaum

Professor Senarath de Alwis

Date _____

The final copy of this thesis has been examined by the signatories, and we find that both the content and the form meet acceptable presentation standards of scholarly work in the above mentioned discipline.

Jensen, Frank (Ph.D., experimental high-energy physics)

Search for supersymmetry using boosted Higgs bosons and missing transverse momentum in proton-proton collisions at 13 TeV

Thesis directed by Professor Kevin Stenson

A search for physics beyond the Standard Model in events with one or more high-momentum Higgs bosons, H , decaying to pairs of b quarks in association with missing transverse momentum is presented. The data, corresponding to an integrated luminosity of 35.9 fb^{-1} , were collected with the CMS detector at the LHC in proton-proton collisions at the center-of-mass energy $\sqrt{s} = 13 \text{ TeV}$. The analysis utilizes a new b quark tagging technique based on jet substructure to identify jets from $H \rightarrow b\bar{b}$. Events are categorized by the multiplicity of H -tagged jets, jet mass, and the missing transverse momentum. No significant deviation from standard model expectations is observed. In the context of supersymmetry (SUSY), limits on the cross sections of pair-produced gluinos are set, assuming that gluinos decay to quark pairs, H (or Z), and the lightest SUSY particle, LSP, through an intermediate next-to-lightest SUSY particle, NLSP. With large mass splitting between the NLSP and LSP, and 100% NLSP branching fraction to H , the lower limit on the gluino mass is found to be 2010 GeV.

Dedications

The taxpayer population.

Contents

Chapter

1	Introduction	1
2	The Standard Model of Particle Physics	3
2.1	Quantum Electrodynamics	4
2.2	Quantum Chromodynamics	5
2.3	Electroweak Theory	6
2.3.1	The Higgs Mechanism	7
2.4	Parameters of the Standard Model	10
3	The Minimal Supersymmetric Model	11
4	The Large Hadron Collider	12
5	The CMS Detector	15
5.1	Silicon Tracker	18
5.1.1	Pixel Detector	18
5.1.2	Strips Detector	19
5.2	Electromagnetic Calorimeter	19
5.2.1	Preshower	20
5.3	Hadronic Calorimeter	20
5.4	Solenoidal Magnet	21

5.5	Muon System	21
5.5.1	Drift Tubes	22
5.5.2	Cathode Strip Chambers	23
5.5.3	Resistive Plate Chambers	23
5.6	Trigger System	23
6	Event Reconstruction	25
6.1	Basic Elements From the Detector	25
6.1.1	Tracker Tracks	25
6.1.2	ECAL Clusters	26
6.1.3	HCAL Clusters	26
6.1.4	Muon Tracks	26
6.2	Obtaining a Particle-level Description	27
6.3	Additional High-Level Objects	29
6.3.1	Jets	29
6.3.2	b-tagging of Jets	30
6.3.3	Neutrinos – Invisible Particles $\rightarrow p_T^{\text{miss}}$	30
6.3.4	π^0 meson	31
7	Search for physics beyond the Standard Model using boosted H bosons and missing transverse momentum in proton-proton collisions at 13 TeV	32
7.1	Motivation & Strategy	32
7.2	Object Definition & Event Selection	34
7.3	Dataset & Trigger	36
7.4	Event Simulation	36
7.4.1	Standard Model Processes	36
7.4.2	Signal Models	38
7.5	Event Binning & Background Estimation	38

7.5.1	Control Regions within Data	41
7.5.2	κ as a Correction to the Estimation	42
7.5.3	Sideband Yields & Predictions	51
7.6	Signal Systematics	52
7.7	Results - Yields in the Signal Regions & Exclusion Curves	56
7.8	Reinterpretation	58
8	Conclusions	63
Bibliography		65

Tables

Table

7.1	SM MC samples used in the analysis.	37
7.2	Summary of the control region scale-factors integrated over p_T^{miss}	45
7.3	Summary of the Single Lepton control region scale-factors in the anti-tag sideband region.	45
7.4	The κ factor computed by throwing Gaussian toys for the scale factors.	49
7.5	Corrected MC Yields in the signal regions.	50
7.6	Corrected MC Yields in each of the signal and sideband regions.	50
7.7	Observed yields in the sideband regions, κ , and background predictions for the 6 signal bins.	52
7.8	Fit results for W-mass resolution in data and MC	54
7.9	Summary of signal shape and normalization uncertainties.	55
7.10	Signal yields and SM background predictions	56
7.11	Comparison of the true reco-level event yield with those obtained via the prediction following the prescription above. The columns with the RECO or GEN labels are the prediction using RECO or GEN event variables only, respectively. The prediction was made using the T5HH MC with a gluino mass of 2200 GeV.	60
7.12	Signal efficiencies for an event to land in a given analysis bin. The efficiencies were derived using the T5HH MC with a gluino mass of 2200 GeV. Choosing a gluino mass of 1800 GeV decreases the efficiencies by a relative 5%.	60

Figures

Figure

1.1	The periodic table of elements.	1
2.1	The particles of the Standard Model.	4
4.1	Nature's source of high-energy particle collisions: a cosmic ray shower.	14
4.2	The LHC complex; 17 miles around, 500ft underground.	14
5.1	A view of the CMS detector.	16
5.2	A view of the CMS detector in the $r\phi$ plane, in the barrel region of the detector.	16
5.3	A view of the CMS detector in the rz plane.	17
5.4	A diagram of a drift tube station.	22
5.5	The CMS L1 trigger system.	24
7.1	Diagrams of the benchmark models used for motivation of the targeted signal.	33
7.2	Distributions of bb-tagging discriminator (top row) and the jet mass (bottom row) for the leading (left column) and subleading (right column) AK8 jets. These are used in H/Z tagging of AK8 jets.	35
7.3	Generator level distributions for the leading (top row) and subleading (bottom row) H boson in the T5HH model. The plot on the left shows the p_T of the H boson. The plot on right shows ΔR between the b-quark daughters - for large H p_T the daughters become collimated.	39

7.4 A diagram of the partitioned phase space. p_T^{miss} binning brings the number of bins to $6 \times 3 = 18$	40
7.5 p_T^{miss} distributions and predictions in the signal regions using simulation only.	41
7.6 Closure observed within the data control regions.	43
7.7 Signal and sideband yields in the single photon control region. The hashed red band denotes the prediction from simulation; the solid black points denote the observed yields in data. The Data/MC ratio in the lower panel of each plot represents the scale factor for that bin.	46
7.8 Signal and sideband p_T^{miss} yields in the single lepton control region. The hashed red band denotes the prediction from simulation; the solid black points denote the observed yields in data. The Data/MC ratio in the lower panel of each plot represents the scale factor for that bin. The low- $\Delta\phi$ requirement has been removed to improve statistics.	47
7.9 Signal and sideband p_T^{miss} yields in the the low- $\Delta\phi$ control region. The hashed red band denotes the prediction from simulation; the solid black points denote the observed yields in data. The Data/MC ratio in the lower panel of each plot represents the scale factor for that bin.	48
7.10 p_T^{miss} distributions and the predictions in the signal regions using simulation with scale factors from data.	49
7.11 p_T^{miss} distribution in each of the control regions comparing data and the scale-factor corrected simulation. The hashed red distribution denote the prediction from simulation; the solid points denote the observed yields in data.	51
7.12 Pruned jet mass in in semi-leptonic $t\bar{t}$ events. The mass peak for the W-jets is used to derive the mass resolution uncertainty.	55
7.13 The single event in the A_2 region.	57
7.14 Observed and expected limits on the gluino cross section.	58

7.15 Efficiencies for an AK8 jet originating from H boson decay, relative to baseline selection. "signal mass" represents the probability the jet will have mass [85, 135 GeV]. "sideband mass" represents the probability the jet will have mass [50, 85 GeV] or [135, 250 GeV]. "H-tag" represents the probability the jet have a double-b discriminator value greater than 0.3, for jets with mass [50, 250 GeV]. Efficiencies were derived using the T5ZH MC with a gluino mass of 2200 GeV.	61
7.16 Efficiencies for an AK8 jet originating from Z boson decay, relative to baseline selection. "signal mass" represents the probability the jet will have mass [85, 135 GeV]. "sideband mass" represents the probability the jet will have mass [50, 85 GeV] or [135, 250 GeV]. "H-tag" represents the probability the jet have a double-b discriminator value greater than 0.3, for jets with mass [50, 250 GeV]. Efficiencies were derived using the T5ZH MC with a gluino mass of 2200 GeV.	62

Chapter 1

Introduction

Perhaps only in passing, many of us have seen images of the periodic table (Figure 1.1) good place to start is with H_2O , colloquially called water. It consists of two hydrogen atoms and one oxygen atom.

The objects responsible for chemistry are found in the periodic table of the elements seen in Figure 1.1. Quantum mechanics was developed in the early 20th century and gave an explanation for the experimentally determined structure to the period table of elements.

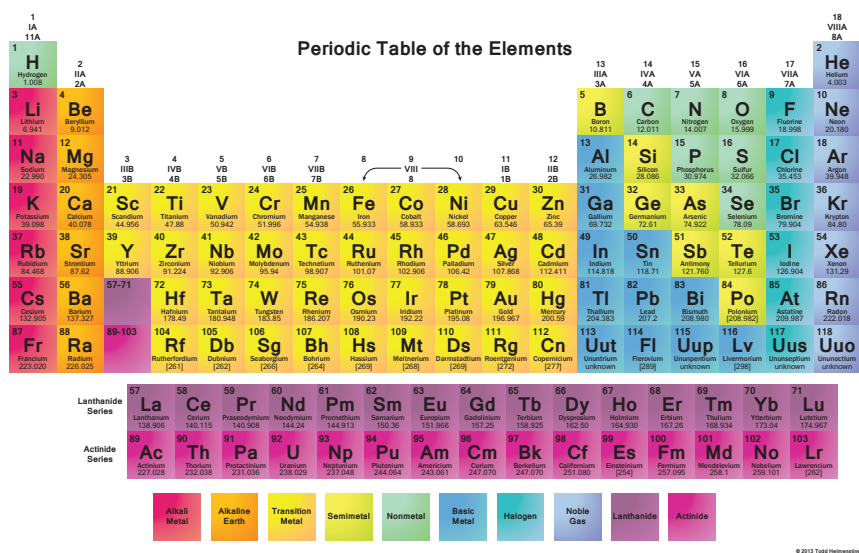


Figure 1.1: The periodic table of elements.

But the elements themselves are made of more fundamental “atoms” described by the Standard Model of particle physics, the current knowledge is summarized in another table, seen in

Figure 2.1.

This thesis gives an overview presents current research in the field of particle physics. A description of the Standard Model is presented in Chapter 2. A description of the Large Hadron Collider (LHC) is presented in Chapter 4. A description of the CMS detector is presented in Chapter 5. A description of the object definition and event reconstruction is presented in Chapter 6. A description of the physics analysis is presented in Chapter 7. The conclusions are discussed in Chapter 8.

Chapter 2

The Standard Model of Particle Physics

The Standard Model of particle physics is the mathematical framework for the description of the fundamental constituents of matter. It provides a quantum mechanical description of the interactions between particles due to three of the four elementary forces: electromagnetism, the weak nuclear force, and the strong nuclear force. Gravitation is the remaining fundamental force, a proper quantum mechanical treatment of it has so far eluded physicists.

The matter particles are divided into *quarks* and *leptons* are listed in Figure 2.1. These are massive spin-1/2 fermions which are represented by solutions to the free-particle Dirac equation generated by the following Lagrangian:

$$\mathcal{L} = i\bar{\psi}\gamma^\mu\partial_\mu\psi - m\bar{\psi}\psi \quad (2.1)$$

Particle interactions are generated by requiring the free-particle Lagrangian to be invariant under the action of different symmetry groups. Demanding local (gauge) invariance requires one to introduce spin-1 vector fields to the Lagrangian which couple with the fermions. The vector fields are to be identified with the generators of the symmetry group and act as the mediator of the force via particle exchange. U(1) generates electromagnetism via interactions with photons. A combination of U(1) and SU(2) generates the electroweak theory, simultaneously describing the electromagnetic and weak nuclear force via interactions with W bosons, Z bosons and photons. SU(3) generates quantum chromodynamics, the theory of the strong nuclear force.

The particles responsible for the transmission of these forces are collectively known as *gauge*

bosons (see Figure 2.1). The massive spin-1 gauge bosons are represented by solutions to the free particle Proca equations generated by the following Lagrangian:

$$\mathcal{L} = -\frac{1}{16\pi}B^{\mu\nu}B_{\mu\nu} + \frac{1}{8\pi}m^2B_\nu B^\nu \quad (2.2)$$

where $B_{\mu\nu} \equiv \partial_\mu B_\nu + \partial_\nu B_\mu$ is known as the *energy-momentum tensor* representing the kinetic energy of the field.

Standard Model of Elementary Particles

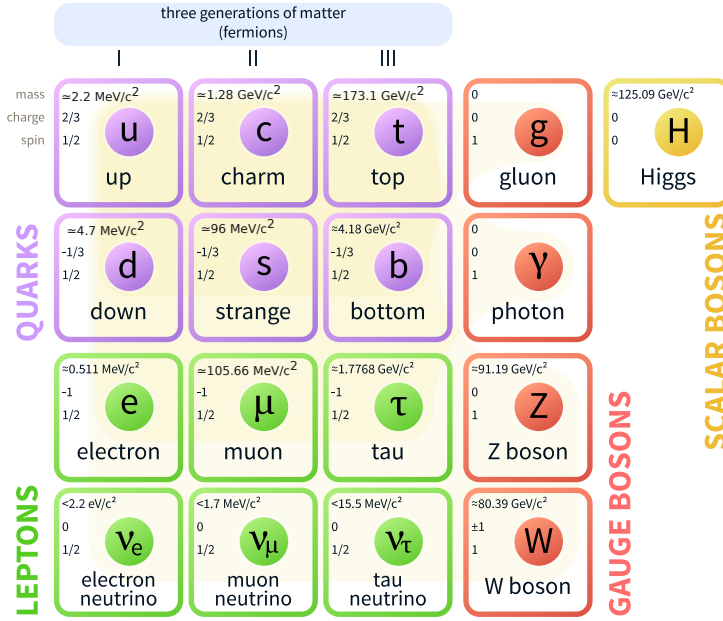


Figure 2.1: The particles of the Standard Model.

2.1 Quantum Electrodynamics

Quantum electrodynamics describes the interactions of particles with electric charge. The interactions arise naturally by requiring the free-particle Dirac Lagrangian to be invariant under the U(1) transformation:

$$\psi(x) \xrightarrow{\text{U}(1)} e^{iq\alpha(x)} \psi(x) \quad (2.3)$$

where q is the electric charge, and α is an arbitrary function of spacetime. ψ is a single Dirac fermion.

$U(1)$ gauge-invariance requires us to modify the definition of the partial derivative to include a spin-1 vector field A_μ , the photon:

$$\begin{aligned}\partial\mu &\rightarrow \partial_\mu - iqA_\mu \\ A_\mu &\xrightarrow{U(1)} A_\mu - q\partial_\mu\alpha\end{aligned}\tag{2.4}$$

The complete Lagrangian becomes:

$$\mathcal{L}_{QED} = i\bar{\psi}\gamma^\mu\partial_\mu\psi - q\bar{\psi}\gamma^\mu\psi A_\mu - m\bar{\psi}\psi - \frac{1}{4}F_{\mu\nu}F^{\mu\nu}\tag{2.5}$$

where $F_{\mu\nu} \equiv \partial_\mu A_\nu - \partial_\nu A_\mu$, is known as the *field strength tensor* and represents the kinetic energy of the photon field. A photon mass term $\frac{1}{2}m^2A^\mu A_\mu$ is forbidden as it is not invariant under the transformation rule.

2.2 Quantum Chromodynamics

Quantum chromodynamics describes the strong force - interactions of particles with color charge. The interactions arise naturally by requiring the free-particle Dirac Lagrangian to be invariant under the $SU(3)$ transformation:

$$\psi(x) \xrightarrow{SU(3)} e^{\frac{1}{2}ig_s\boldsymbol{\alpha}(x)\cdot\boldsymbol{\lambda}}\psi(x)\tag{2.6}$$

where g_s is the strong coupling constant, $\boldsymbol{\alpha}$ is an arbitrary 8-dimensional vector of spacetime, and $\boldsymbol{\lambda}$ are the 8 3x3 Gell-Mann matrices. ψ is a color triplet of Dirac fermions $\bar{\psi} = (\psi_{red}, \psi_{blue}, \psi_{green})$.

$SU(3)$ gauge invariance requires us to modify the definition of the partial derivative to include 8 spin-1 vector fields G_μ , the gluons:

$$\begin{aligned}\partial\mu &\rightarrow \partial_\mu - ig_s\boldsymbol{\lambda}\cdot\boldsymbol{G}_\mu \\ G_\mu^k &\xrightarrow{SU(3)} G_\mu^k - g_s\partial_\mu\alpha_k - g_sf_{ijk}\alpha_iG_\mu^j\end{aligned}\tag{2.7}$$

where f_{ijk} are known as the *structure constants* of $SU(3)$ and arise from its non-abelian nature, they satisfy $[\lambda_i, \lambda_j] = 2if_{ijk}\lambda_k$. This term is responsible for the self-coupling within the gluon field.

The complete Lagrangian becomes:

$$\mathcal{L}_{\text{QCD}} = i\bar{\psi}\gamma^\mu\partial_\mu\psi - (g_s\bar{\psi}\gamma^\mu\lambda\psi)\cdot\mathbf{G}_\mu - m\bar{\psi}\psi - \frac{1}{16\pi}\mathbf{G}^{\mu\nu}\cdot\mathbf{G}_{\mu\nu} \quad (2.8)$$

where $G_i^{\mu\nu} \equiv \partial^\mu G_i^\nu - \partial^\nu G_i^\mu - 2q f_{ijk} G_j^\mu G_k^\nu$ is the field strength tensor for the gluon fields.

The presence of the gluon mass term $\frac{1}{2}m^2\mathbf{G}^\mu\cdot\mathbf{G}_\mu$ is forbidden as it is not invariant under the transformation rule and they remain massless.

2.3 Electroweak Theory

Electroweak theory is a quantum field theory which provides a description of the weak nuclear force between particles with *weak isospin* and *hypercharge* quantum numbers. In concert with this description comes that of electrodynamics, thereby uniting the two in a single framework. The theory is generated by demanding local invariance of the Lagrangian under a combined $SU(2)\times U(1)$ symmetry. Four new gauge fields must be introduced into the theory to give the proper transformation rule of the covariant derivative. Mixing between these fields generates the physical W^\pm boson, Z boson, and photon. Under $SU(2)\times U(1)$, the fields transform in the following manner:

$$\begin{aligned} \psi(x) &\xrightarrow{U(1)} e^{ig'\frac{Y}{2}\alpha(x)} \psi(x) \\ \psi_L(x) &\xrightarrow{SU(2)} e^{ig_W\xi(x)\cdot\frac{1}{2}\sigma} \psi_L(x) \end{aligned} \quad (2.9)$$

where g' is the hypercharge coupling constant, Y is the hypercharge operator, g_W is the weak coupling constant, α and ξ are arbitrary functions of spacetime, and σ represents the 3 2x2 Pauli spin matrices. ψ_L is an **isospin doublet** made of the following fermion anti-fermion pairs:

$$\begin{pmatrix} \nu_e \\ e \end{pmatrix}, \begin{pmatrix} \nu_\mu \\ \mu \end{pmatrix}, \begin{pmatrix} \nu_\tau \\ \tau \end{pmatrix}, \begin{pmatrix} u \\ d' \end{pmatrix}, \begin{pmatrix} c \\ s' \end{pmatrix}, \begin{pmatrix} t \\ b' \end{pmatrix}$$

The weak force is a *chiral* theory which does not treat the left and right-chiral components of a Dirac fermion equally. The projection operator $P_{R,L} = \frac{1}{2}(1 \pm \gamma^5)$ defines these states and all fermions can be decomposed as $\psi = \psi_L + \psi_R$. Within the electroweak theory, isospin doublets consist of pairs of left-chiral particles and right-chiral antiparticles.

As usual, SU(2) and U(1) gauge-invariance requires us to modify the definition of the partial derivative to include three spin-1 vector fields \mathbf{W}^μ and a single spin-1 vector field B^μ :

$$\begin{aligned}\partial\mu &\rightarrow \partial_\mu - ig' \frac{Y}{2} B_\mu - ig_W \frac{1}{2} \boldsymbol{\sigma} \cdot \mathbf{W}_\mu \\ B_\mu &\xrightarrow{\text{U}(1)} B_\mu - ig' \partial_\mu \alpha \\ W_\mu^k &\xrightarrow{\text{SU}(2)} W_\mu^k - g_W \partial_\mu \alpha^k - g_W \epsilon_{ijk} \xi^i W_\mu^j\end{aligned}\tag{2.10}$$

where ϵ_{ijk} is the totally antisymmetric Levi-Civita tensor (the structure constants of SU(2)).

Because of the SU(2) symmetry, we must introduce **two** Dirac fermions to the theory, where the left and right chiral components are treated differently. Without loss of generality we will label these fields at $\bar{\psi} = (\chi \xi)$, but these can be any of the available pairs listed above. The Lagrangian will be written in terms of these new fields:

The complete Lagrangian becomes:

$$\begin{aligned}\mathcal{L}_{\text{EWK}} = &i\bar{\chi}\gamma^\mu\partial_\mu\chi - m\bar{\chi}\chi + i\bar{\xi}\gamma^\mu\partial_\mu\xi - m\bar{\xi}\xi - \frac{1}{4}B_{\mu\nu}B^{\mu\nu} - \frac{1}{4}\mathbf{W}_{\mu\nu}\cdot\mathbf{W}^{\mu\nu} \\ &- g'\bar{\chi}\gamma^\mu\frac{Y}{2}\chi B_\mu + g'\bar{\xi}\gamma^\mu\frac{Y}{2}\xi B_\mu - g_W\bar{\psi}\gamma^\mu\boldsymbol{\sigma}\psi\cdot\mathbf{W}_\mu\end{aligned}\tag{2.11}$$

The B^μ and \mathbf{W}^μ bosons remain massless as mass terms would not be invariant under the symmetry transformation rule for the vector fields. The observable W and Z bosons are indeed massive, so mass terms must be generated through some other mechanism.

2.3.1 The Higgs Mechanism

As has been mentioned, the gauge bosons in the electroweak theory must remain massless as the appropriate term in the Lagrangian would not remain invariant under the transformation rule of the field. Additionally, it has not been mentioned that the fermion mass terms $-m\bar{\psi}\psi = -m(\bar{\psi}_R\psi_L + \bar{\psi}_L\psi_R)$ are forbidden as they are not invariant under the chiral-transformation of the theory treating the left and right-chiral components differently. The Higgs mechanism is able to generate mass terms for the W, Z, and fermions within the Standard Model. This is an essential component and its discovery in 2012 was monumental. [1]

This Higgs mechanism proceeds by introducing a massive spin-0 complex scalar field with the following Lagrangian.

$$\mathcal{L} = \frac{1}{2}(\partial_\mu\phi^\dagger)(\partial^\mu\phi) - \frac{1}{2}\mu^2\phi^\dagger\phi + \lambda(\phi^\dagger\phi)^2 \quad (2.12)$$

where μ and λ are the strengths of the self-coupling terms.

The field in the Standard Model is in fact an isospin doublet consisting of electrically neutral and charged components:

$$\phi = \begin{pmatrix} \phi^+ \\ \phi^0 \end{pmatrix} = \begin{pmatrix} \phi_1 + i\phi_2 \\ \phi_3 + i\phi_4 \end{pmatrix}, \quad (2.13)$$

Solving for the minimum of the potential, it is found that the ground state of ϕ is non-zero and satisfies $\phi^\dagger\phi = \phi_1^2 + \phi_2^2 + \phi_3^2 + \phi_4^2 = \frac{v^2}{2} = -\frac{\mu^2}{2\lambda}$. As particles are represented as fluctuations above the vacuum, we must express the fields in the same manner. Electric charge conservation requires that this *vacuum expectation value* lie entirely inside the neutral ϕ^0 which is rewritten as $\phi^0 = v + h(x)$, where $h(x)$ is to be identified as the Higgs boson.

2.3.1.1 Masses of the W and Z bosons

The kinetic energy term $\frac{1}{2}(\partial_\mu\phi^\dagger)(\partial^\mu\phi)$ for the Higgs boson introduces a coupling with the \mathbf{W}^μ and \mathbf{B}^μ bosons when they are added to the covariant derivative:

$$\partial_\mu\phi = \left(\frac{1}{2}\partial_\mu + \frac{1}{2}ig_W\boldsymbol{\sigma} \cdot \mathbf{W} + ig'\frac{Y}{2}B^\mu \right) \begin{pmatrix} 0 \\ v + h(x) \end{pmatrix} \quad (2.14)$$

After performing the matrix calculations, and lots of algebra, we see there are terms quadratic in the gauge fields:

$$\frac{1}{8}v^2g_W^2(W_\mu^1W_1^\mu + W_\mu^2W_2^\mu) + \frac{1}{8}v^2(g_WW_\mu^3 - g'B_\mu)(g_WW_3^\mu - g'B^\mu) \quad (2.15)$$

Where we see we have generated mass terms for the $\mathbf{W}_{1,2}^\mu$ fields: $\frac{1}{2}v^2g_W^2W^\mu W_\mu$. The last term in the expansion introduces mixed couplings between the \mathbf{W}_3^μ and \mathbf{B}^μ fields and the term can

be represented as a mass matrix with non-diagonal entries - physical particles are eigen states of the mass matrix. Upon diagonalization, we find the states corresponding to the physical particles:

$$\begin{aligned} A_\mu &= \frac{1}{\sqrt{g_W^2 + g'^2}} (g' W_\mu^3 + g_W B_\mu); & \text{with mass } 0 \\ Z_\mu &= \frac{1}{\sqrt{g_W^2 + g'^2}} (g_W W_\mu^3 - g' B_\mu); & \text{with mass } \frac{1}{2} v \sqrt{g_W^2 + g'^2} \end{aligned} \quad (2.16)$$

where A_μ corresponds to the photon of electromagnetism, and Z_μ the neutral gauge boson responsible for the weak neutral currents.

The physical W bosons are in fact linear combinations of the W^μ fields: $W_\mu^\pm = \frac{1}{\sqrt{2}} (W_\mu^1 \pm W_\mu^2)$.

These correspond to the raising and lowering operators of SU(2) and therefore step between states with differing isospin component I_3 , indicated in the doublet pairings seen above.

We have seen how the Higgs mechanism is able to generate mass terms for the gauge bosons in the electroweak theory.

2.3.1.2 Masses of the Fermions

Up to this point, it has not been mentioned that the fermion mass term $m\psi\bar{\psi}$ is not invariant under the SU(2) symmetry - the left-chiral states transform as isospin doublets whereas the right-chiral states transform as singlets. This is made explicit by using the projection operators to decompose a Dirac fermion into left and right chiral components $-m\bar{\psi}\psi = -m(\bar{\psi}_L\psi_R + m\bar{\psi}_R\psi_L)$. As the fermion masses are all non-zero, some mechanism must be built into the Standard Model to generate mass terms. This is done by introducing an interaction between the Higgs field and fermions. Consider the following Lagrangian:

$$\mathcal{L} = -y(\bar{\psi}_L\phi\psi_R + \bar{\psi}_R\phi^\dagger\psi_L) \quad (2.17)$$

where y is the *Yukawa coupling*, $\bar{\psi}_L$ is an isospin doublet of left-chiral fermions, and ψ_R is a right-chiral fermion.

2.4 Parameters of the Standard Model

Throughout this chapter we have encountered 15 parameters that must be specified as an input to the theory which must all be determined experimentally. Here is the list:

- the 9 quark and lepton masses: $m_u, m_d, m_s, m_c, m_b, m_t, m_e, m_\mu, m_\tau$
- 4 CKM matrix elements, often parametrized by λ, A, ρ, η
- the Higgs mass and quartic coupling: m_H, λ

Inclusion of massive neutrinos in the theory creates an additional 7 parameters:

- three neutrino mass eigenstates: $m_{\nu_1}, m_{\nu_2}, m_{\nu_3}$
- four parameters for the PMNS matrix, governing mixing between the neutrino mass and flavor states (analogous to the CKM matrix).

Although the exact implementation of their masses in the SM is unknown.

Chapter 3

The Minimal Supersymmetric Model

This section has been adapted from [2].

Chapter 4

The Large Hadron Collider

The Standard Model provides a framework for understanding the fundamental particles and the underlying forces which govern their behavior. Among other things, the SM is very successful at modeling scattering amplitudes and decay rates.

Nature itself has provided us with a source of high-energy particle collisions in the form of cosmic rays. Cosmic rays are very high energy protons and light atomic nuclei which originate from outside the Solar System. When they enter our atmosphere, they collide with the (primarily) nitrogen, oxygen, or argon atoms causing them to break apart creating showers of particles within the atmosphere. As the particles rain down on Earth, many of them decay into less massive ones or are absorbed in the atmosphere - muons and neutrinos are the only particles which make it to the surface. A diagram of this phenomena is seen in Figure 4.1. Indeed there are many experiments which set out to detect cosmic ray showers, but at the LHC a different approach is taken and we build machines on Earth to generate the particle collisions - although at not nearly such large energies provided by extrastellar space. The particle collisions can be focused to a single part of space, the region around the beam spot can be extensively instrumented to detect the debris of the collision.

The Large Hadron Collider (LHC) is a facility which houses two beams of protons (each beam centimeters in transverse size) running parallel in an underground ring 17 miles in circumference. The protons are accelerated to nearly the speed of light by electric fields and are steered within their circular trajectory using magnetic fields generated by superconducting magnets. A schematic

of the complex which houses this machine is seen in the left panel of Figure 4.2; as seen in the diagram, the LHC is the final machine of a number of stages which each incrementally increase the energy of the protons. There are 5 locations around the ring where the beams are crossed and particle detectors are placed. The right panel of Figure 4.2 shows the LHC complex underground near Geneva, Switzerland.

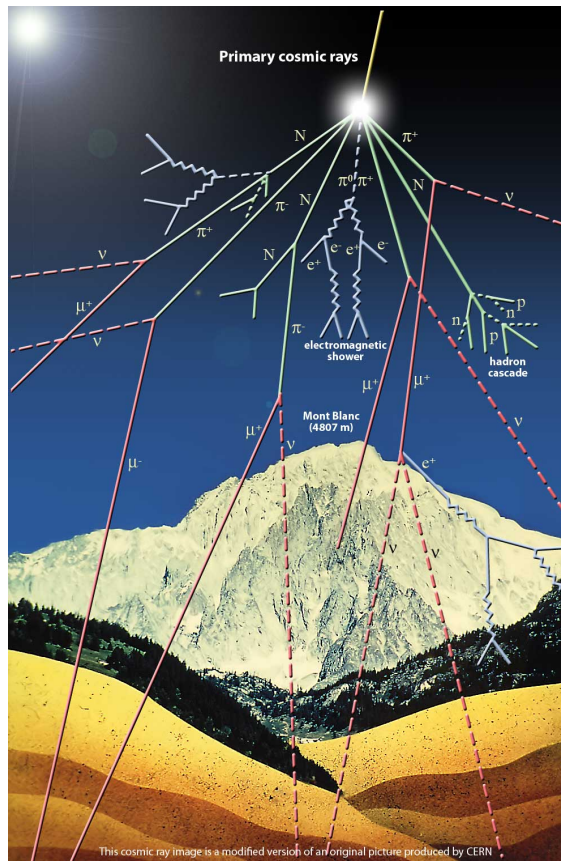


Figure 4.1: Nature's source of high-energy particle collisions: a cosmic ray shower.

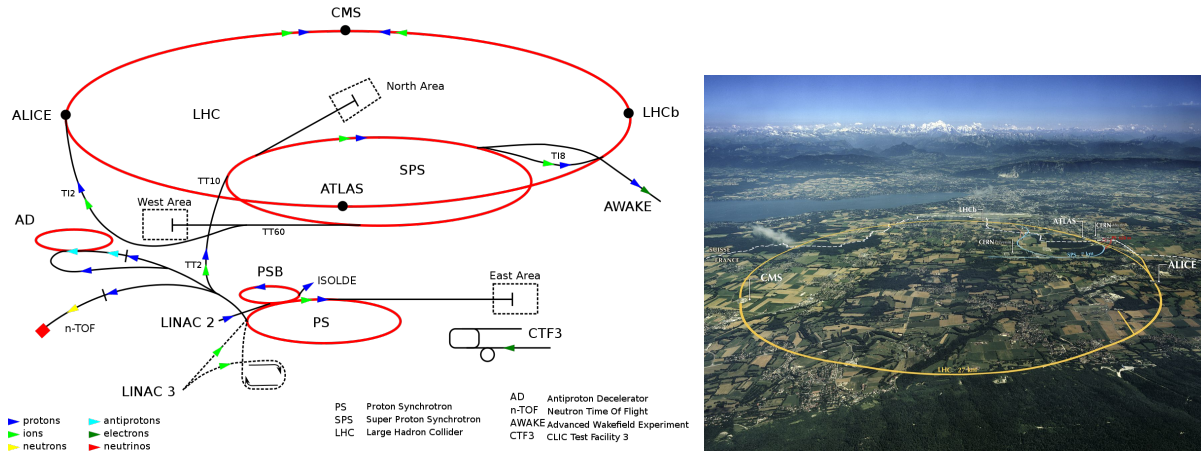


Figure 4.2: The LHC complex; 17 miles around, 500ft underground.

Chapter 5

The CMS Detector

To ensure as much as possible of the debris of the proton-proton collisions can be detected, CMS is constructed to maximize the solid-angle coverage of the interaction region. The 20 cm transverse size of the beam-pipe prohibits instrumentation in the most forward of this region. CMS is composed of a modular design of different detectors, each with their own technology and working points, allowing for direct measurements of a wide spectra of particles. The detector can generically be divided into central *barrel* and forward *endcap* regions. The geometry either takes the form of concentric cylinders (in the barrel) or flat planes of detectors (in the endcaps). Figure 5.3 illustrates the barrel ($|\eta| < 1.5$) and endcap ($1.5 < |\eta| < 5$) regions, the beamline is seen as the thin cyan line across the base of the image.

Only the lightest particles have a long enough lifetime to travel any appreciable distance within our detector. Electrons e^\pm , photons γ , and protons p^\pm are stable and can be directly detected within CMS. In addition, muons μ^\pm , pions π^\pm, π^0 , neutrons n, and kaons K^\pm, K^0 all have long enough lifetimes to be directly detected. Neutrinos ν do not interact at all within our detector, they create an imbalance in the total momentum of the event. All other particles produced during the collisions must be reconstructed from these.

This chapter will discuss the main elements of the CMS detector, beginning with the innermost (closest to the beam pipe) silicon tracker and concluding with the muon tracker.

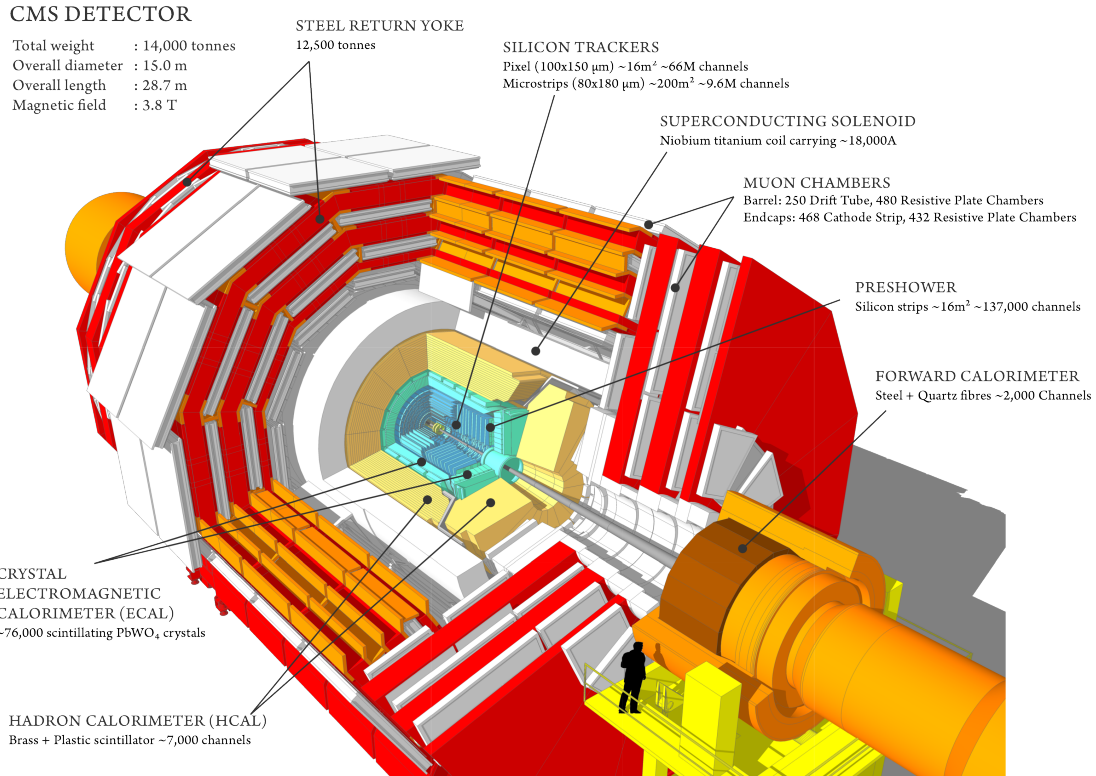
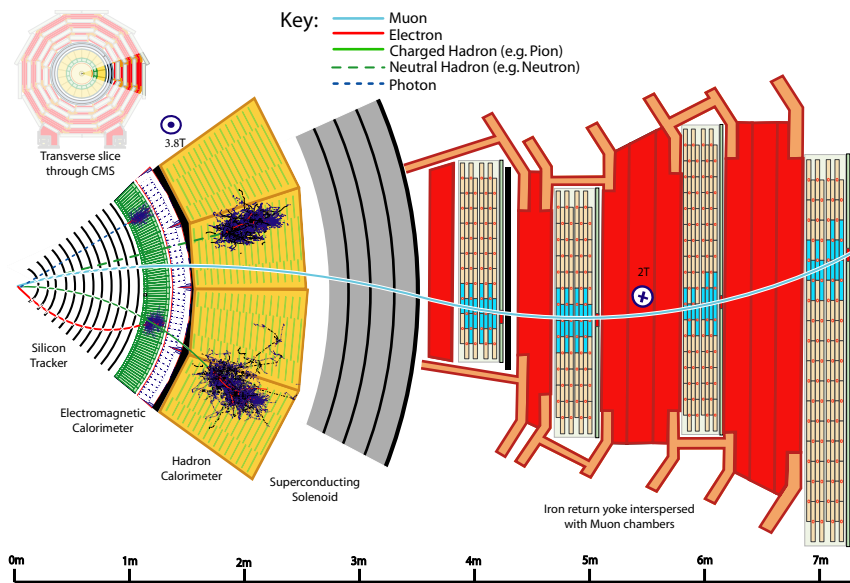


Figure 5.1: A view of the CMS detector.

Figure 5.2: A view of the CMS detector in the $r-\phi$ plane, in the barrel region of the detector.

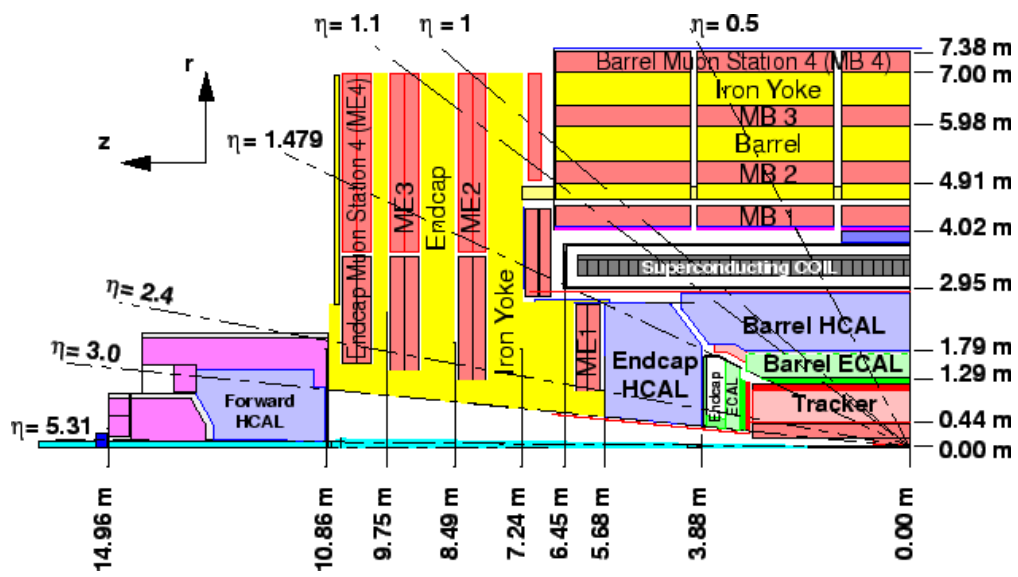


Figure 5.3: A view of the CMS detector in the r - z plane.

5.1 Silicon Tracker

The silicon tracker is responsible for the reconstruction of charged particles: electrons, muons, kaons and pions. The particle trajectory is reconstructed using ionization deposits left in layers of thin silicon. The particle momentum is measured by the curvature of the trajectory when submerged in the magnetic field.[3] [4]

The tracker is built of modules consisting of a reversed-biased, fully-depleted, silicon p-n junction. As a charged particle travels through the material, it ionizes the silicon creating electron-hole pairs within the depletion zone. Electric fields accelerate the charge through the silicon and to the readout electronics bonded to the back of the sensor where the signal is then amplified and digitized, before being piped outside the detector. The silicon is very thin ($300\mu\text{m}$), the tracker is constructed of as little material as possible so as not to perturb the original trajectory of the particle.

The silicon tracker is divided into two major components. The pixel detector is at a closer proximity to the beam line and has finer spatial segmentation. The strips detector covers a larger spatial volume and is responsible for the majority of the hits along a particle trajectory.

5.1.1 Pixel Detector

The task of the pixel detector is to provide the spatial granularity required for precision track vertexing (importance will be discussed in Chapter 6). The barrel region ($|\eta| < 1.5$) of the pixel detector consists of 4 concentric cylinders sitting at radii between 2.9 and 16 cm from the beamline. The endcaps ($1.5 < |\eta| < 2.5$) consist of three discs on each side ($\pm z$) placed in between $z = 3.2$ and 4.8cm. The silicon modules are pixelated into elements $100 \times 150\mu\text{m}$ wide, yielding more than 65 million individual readout channels.

5.1.2 Strips Detector

The silicon strips sit immediately outside the pixel detector and provides additional hits along a particle's trajectory: the barrel region ($|\eta| < 1.5$) provides 10 layers, the endcaps ($1.5 < |\eta| < 2.5$) provide 12. The silicon modules are partitioned in strips ranging from $80 - 180 \mu\text{m}$ wide, yielding more than 10 million individual readout channels.

5.2 Electromagnetic Calorimeter

The electromagnetic calorimeter is responsible for the reconstruction of electrons e^\pm , photons γ and charged pions π^\pm . The energy is measured by collecting the light generated by an electromagnetic shower as the particle is absorbed in the calorimeter.[5][6]

The bulk of the calorimeter consists of lead-tungstate (PbWO_4) crystal. Electromagnetic showers are created when high energy particle enters the material. Low-mass particles, such as electrons, scatter as they traverse the material and emit bremsstrahlung radiation in the form of lower-energy photons. Photons interact with the material and convert into an electron-positron pair, which themselves are able to then emit radiation. The light generated by this shower is collected using photodetectors mounted at the end of each crystal. Light incident on the photodetector first encounters silicon where the photon knocks an electron of a silicon atom. This electron is accelerated with an electric field onto an electrode surface which liberates electrons via the photoelectric effect. These electrons are accelerated onto another electrode which in turn liberate more electrons. This signal is then further amplified and digitized.

The electromagnetic calorimeter is divided into barrel ($|\eta| < 1.5$) and endcap ($1.5 < |\eta| < 3$) regions comprising over 75,000 crystals. The crystals measure $2.2 \times 2.2 \times 23 \text{ cm}$ in the barrel (matching the Moliere radius of PbWO_4 - 2.2 cm) and $3 \times 3 \times 22 \text{ cm}$ in the endcaps; they are oriented radially outward from the interaction region. This thickness of absorber is sufficient to contain over 98% of the energy of incident particles. Additionally, the electromagnetic calorimeter serves as an absorber for the hadronic calorimeter, initiating a shower in approximately 1/3 the particles headed

for the hadronic calorimeter.

5.2.1 Preshower

The Preshower is a more finely segmented region of the electromagnetic calorimeter intended for greater spatial resolution for resolving electromagnetic showers. It consists of two alternating layers of lead absorber and Si detectors (like the tracker) which are able to reconstruct the electron-positron pairs created at an early stage in the showering process. The silicon detector is able to reconstruct the electron and positron trajectories allowing for the greater spatial resolution compared to the rest of the calorimeter.

The motivation for the Preshower is for the proper identification of high- p_T neutral pion decay (98.8% branching fraction to two photons). The Preshower only exists in a forward region $1.7 < \eta < 2.6$ where this poses the greatest challenge because of the pion kinematics.

5.3 Hadronic Calorimeter

The hadronic calorimeter is responsible for the reconstruction of hadrons: charged pions π^\pm , protons p^\pm , neutrons n , and kaons K^\pm, K^0 . The particle energy is measured by collecting light generated by a hadronic shower as the particle is absorbed in the calorimeter.[7]

The bulk of the calorimeter consists of steel and brass absorber. A particle will interact with the material causing a shower of a number of secondary particles. These secondary particles in turn interact and this process creates a particle shower within the detector. Interspaced with the absorber are tiles of clear plastic scintillator which create flashes of light after de-excitation of the scintillating molecules embedded in the plastic. Fibers are ran throughout the plastic and absorb the light, which is then piped to hybrid photodiodes. Light incident on the photodiodes liberates electrons via the photoelectric effect which are then accelerated onto the surface of a silicon diode which further amplifies and digitizes the signal.

The hadronic calorimeter is divided into barrel ($|\eta| < 1.2$), endcap ($1.2 < |\eta| < 3$), and forward regions ($1.2 < |\eta| < 3$) and contains over 9000 readout channels. In all regions the absorber

is over a meter thick and consists of many layers of plates about 5cm thick. The scintillator plates are about 1cm thick. This thickness of absorber is sufficient to contain over 98% of the energy of incident particles. There is an additional section of calorimeter in the barrel region which sits outside the magnet solenoid and detects late-starting showers.

5.4 Solenoidal Magnet

The CMS magnet provides the field necessary to deflect charged particles within the trackers to allow for a measurement of the momentum. The superconducting iron electromagnet delivers a uniform 3.8 T solenoidal field (parallel to the beampipe) within the silicon tracker volume. The magnetic field lines are returned via steel yokes sitting outside the magnet interspaced within the muon tracker volume, the field strength throughout the muon system is approximately 2 T. [8].

5.5 Muon System

The muon system is responsible for the reconstruction (and triggering) of muons μ^\pm . The muon trajectory is reconstructed using ionization deposits left in layers of gaseous detectors. The muon momentum is measured by the curvature of the trajectory when submerged in the magnetic field.[9]

The muon detectors sit at the furthest distance from the beamline, and any particles which have made the journey traveled through many layers of detector material (e.g. silicon Si, lead tungstate PbWO₄, brass (Cu), iron Fe) before being detected. Because of the relatively long lifetime and large mass of the muon they are the only particles which are expected to reach the muon detectors.

There are three components of the muon detector: drift tubes, cathode strip chambers, and resistive plate chambers. The drift tubes and cathode strip chambers are primarily used for tracking in the barrel endcap regions, respectively. There is a small amount of overlap in coverage of the two subdetectors. The resistive plate chambers are used primarily for triggering and has coverage in the barrel and endcap regions, instrumented within the drift t bins and cathode strip chambers.

5.5.1 Drift Tubes

The drift tubes are used for muon tracking in the barrel portion of the detector ($|\eta| < 1.3$). The basic element is a gas tube 4×1.3 cm in transverse size and 2-4 m long (depending on its position). High-voltage is applied to a wire strung the length of the cylinder and collects charge released when an incident muon ionizes the gas mixture. For economic and safety reasons the gas mixture is chosen to be Ar and CO₂. An 85/15% fraction is chosen for nice gas quenching (shower avalanche) and drift velocity properties. [10]

The drift tubes are divided into four barrel regions (each called a station) at different radii within the magnetic return yoke. Each station contains 3 *superlayers*, where a superlayer is composed of four layers of stacked tubes, each layer staggered by one half width. For each station, two of the superlayers are oriented parallel to the beamline for $r - \phi$ measurements and one superlayer is perpendicular to the beamline to allow for measurements of the r-z position. An image of a DT station is seen in Figure 5.4.

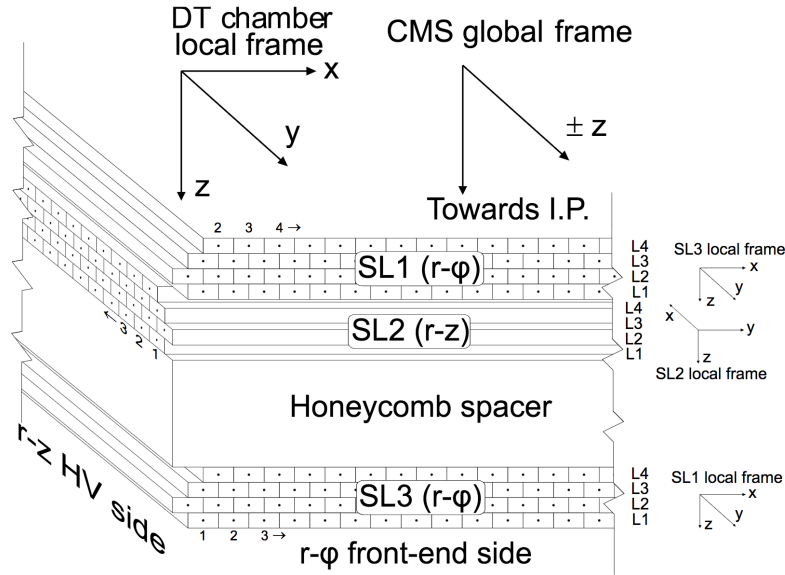


Figure 5.4: A diagram of a drift tube station.

5.5.2 Cathode Strip Chambers

The cathode strip chambers are used for muon tracking in the endcap portion of the detector ($0.9 < |\eta| < 2.4$). The system is divided up into 468 trapezoidal chambers arranged in concentric rings on each disk - 4 discs on each side $\pm z$. Each chamber consists of 6 layers of electrode planes separated by a gas layer of $C_2H_2F_4$ (freon) and C_4H_{10} (isobutane). Wires are strung through the chamber to collect the electrons released when a muon ionizes the gas. One electrode plane is segmented in strips perpendicular to the wires, a readout of the image charge provides a measurement in this other dimension. The segmented strips are oriented in the x-y plane, the wires are oriented in the z plane. [11]

5.5.3 Resistive Plate Chambers

Resistive plate chambers cover the entire region within $|\eta| < 2.5$ and are interspersed within the other muon detectors and the magnetic return yoke. They have an excellent timing resolution of 3ns which allows for fast muon triggering and identification of the different bunch crossings. Pattern matching across the hits in the different layers allows for estimates of the muon p_T to be used in further trigger processing. Hits created in the resistive plate chambers are additionally used for global fitting of the muon tracks.

The resistive plate chambers consist of an airtight system of two parallel high-resistivity planes separated by a 1cm gas gap. The outside of each plate is coated to form an electrode for the high-voltage bias. On top of each electrode sits aluminum strips which are insulated from the electrode and serve as the readout. Electron showers created in the gas bulk induce an image charge on the strips.

5.6 Trigger System

While in operation mode, the LHC provides collisions at a rate of 400 MHz (25ns per bunchcrossing). This is a phenomenal rate which the CMS detector bandwidth is not able to

accommodate, nor does the experiment have access to the amount of disc space necessary to store all this information. Therefore, the CMS detector makes use of a trigger system to quickly determine if the event is 'interesting' and will be saved for storage - events which are not triggered are lost forever. Examples of interesting events contain those with high- p_T muons, or a large imbalance in the total momentum of the event.[12]

The trigger consists of two stages known as the Level-1 (L1) and High-Level Trigger (HLT). L1 is a hardware based trigger which combines information from the calorimeters and muon systems to make a decision if the event will be passed to HLT for further processing. L1 is able to reduce the event rate from 400 MHz to 100 kHz and must make the decision within $4\mu s$. Primitive objects such as calorimeter energy deposits or muon track segments are first constructed locally within the detector before being combined to form the global decision at L1. The flowchart seen in Figure 5.5 illustrates the L1 system. If the decision is made at L1 that the event is of potential interest, it is passed to HLT. HLT is a software based trigger which makes use of more sophisticated reconstruction algorithms which can be tuned to select events of choice.

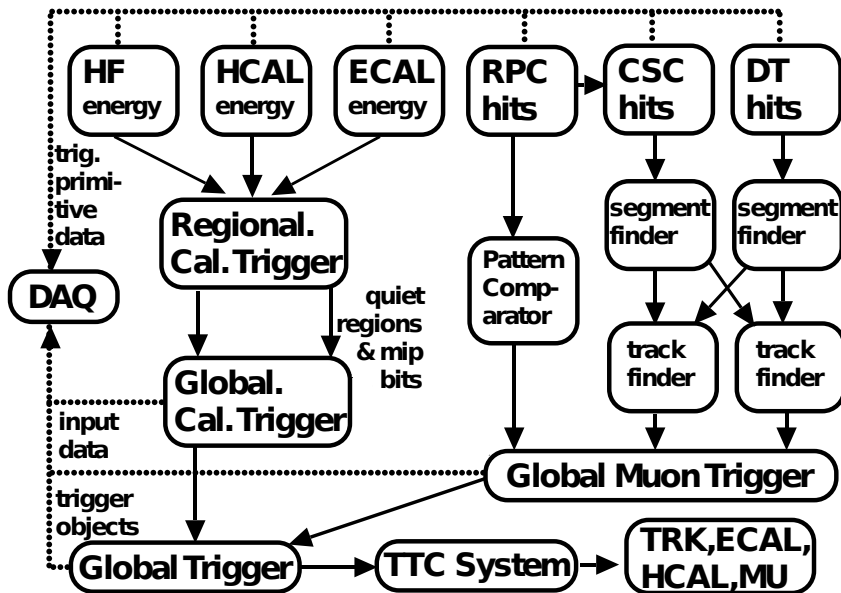


Figure 5.5: The CMS L1 trigger system.

Chapter 6

Event Reconstruction

6.1 Basic Elements From the Detector

Depending on their nature, the particles emanating from the collision leave various forms of energy deposits in the different subdetectors. All these signals need to be aggregated and processed to allow for the reconstruction of what could be considered particle-level information. The first step in this process consists of building *Particle Flow elements* using information only locally within each subdetector. There are four primary elements from the subdetectors: tracks from the tracker, calorimeter deposits in each the ECAL and HCAL, and tracks from the muon detector. As will be discussed in the next section the elements are combined via the Particle Flow *algorithm*, yielding reconstructed particles used for physics analysis.

Note that the definition of any object within the detector makes use of additional selection criteria which is not generally discussed here. For instance, one may require that a track in the tracker have at least 3 hits in the pixel detector, or that a calorimeter hit is above some minimum threshold energy. The effects of this selection is generally a balance between the reconstruction efficiency of any given particle and the probability to misidentify a particle (purity).

This chapter is adapted from [13].

6.1.1 Tracker Tracks

Track seeds are formed separately in the Pixel and Strips detectors by clustering adjacent elements. This creates a reconstructed hit in that detector layer. Charge sharing among pixels in

the hit allows a finer resolution as the position can be better determined using a charge weighted sum of hit coordinates.[14]

6.1.2 ECAL Clusters

Superclusters are built by first identifying a crystal with the largest energy deposit, this is called a *seed*. The supercluster is then formed by aggregating any hits among the neighbors (8) of the hits already in the cluster. This process then proceeds building all the superclusters and consuming all the calorimeter hits. Superclusters are built separately in the barrel and endcap. Within a given supercluster, N clusters are identified using an iterative algorithm assuming the observed hits arise from N Gaussian-distributed energy deposits; each of energy E, position in the $\eta - \phi$ plane $\vec{\mu}$, and width σ scale set by the crystal size.

6.1.3 HCAL Clusters

6.1.4 Muon Tracks

As there are multiple detector layers within a single muon station, track segments are locally formed within a chamber for both the DTs and CSC. These track segments represent the muon momentum at that station; pattern recognition is able to provide to measurement and its high speed allows the segments to be used trigger primitives for the muon systems, as was seen in Figure 5.5. For track reconstruction, the track segments act as seeds for the track finding algorithm. The hits in each the DT, CSC, and RPC subdetectors are used in the final track reconstruction.

The geometry of the DT system allows for up to 32 measurements of the $r-\phi$ position and 16 for the $r-z$. The geometry of the CSC system allows for any in between 20-28 hits, depending on the position η . The geometry of the RPC system allows for any in between 6-10 hits, depending on the position η .

6.2 Obtaining a Particle-level Description

Once the elements have been built, the Particle Flow algorithm exploits the information from each of the detectors to form the best possible particle candidate. [13]. As different varieties of particles have unique signatures in the detector, particle identification is aided by the particular combination of elements *linked* with one another. An illustrative example of these combinations we have seen in Figure 5.2 Elements are linked when projections from one element to the other are spatially consistent. There are four primary links:

- Tracks formed in the tracker are linked to an ECAL or HCAL cluster if the projection of the track, at a depth of the expected maximum of a shower in the ECAL or at one interaction length inside the HCAL, lies within the cluster area.
- ECAL and HCAL clusters are linked if the ECAL cluster falls within the envelope of the HCAL cluster; ECAL provides finer spatial resolution compared to the HCAL.
- A tracker track and a muon track are linked if their projections onto a common surface are spatially consistent.
- To collect bremsstrahlung radiation (photons) associated to an electron track, an ECAL cluster is linked to tracker tracks if projections tangent to the track at any of the tracker layers lies within the cluster volume. Additionally, as the probability for a photon to convert to an e^+e^- pair is significant (XX%) within the tracker, track pairs are linked if they are consistent with photon conversion.
- If a Preshower cluster is within the envelope of an ECAL cluster the two are linked; Preshower has finer spatial granularity.
- Tracks consistent with arising from a secondary vertex are linked to allow for reconstruction of nuclear-interactions.

Particle Flow *blocks* are constructed by aggregating objects directly or indirectly linked with one another. The Particle Flow algorithm then processes each block in turn to create the final reconstructed particles. The algorithm builds the objects in the following order

(1) **Muons:** There are three types of tracks which can be used for muon reconstruction:

- ***standalone*** muons are built from tracks reconstructed solely in the muon system.
- ***tracker*** muons are built from tracks reconstructed solely in the inner silicon tracker. It is tagged as being from a muon if, when projected onto a common surface, it is spatially consistent with a muon solely reconstructed from the muon chambers. Tracker muons have the best resolution for muons up to a p_T of 200 GeV, as these are more likely to suffer from multiple scattering before enter the muon chambers.
- ***global*** muons are reconstructed using the hits from both the inner silicon tracker and the muon stations. The track pairing is the same done for tracker muons. For momenta above 200 GeV, the use of the muon system for tracks improves the momentum measurement.

Any ECAL or HCAL clusters associated with the muon track are used as muon selection/definition criteria if those clusters are found to be consistent with the muon hypothesis (what does this mean?).

(2) **Electrons & Isolated Photons:**

An electron is formed by combining a track in the silicon tracker with a cluster in the ECAL. Its energy assignment uses a combination of both elements. The momentum direction is made using the track in the silicon tracker, as it gives greater spatial resolution. A photon is defined as an ECAL cluster not associated with a track. Photon isolation is a requirement on the sum of the track p_T within a cone $\Delta R = 0.3$ around the photon; photons which arise during hadron fragmentation (i.e. poor isolation) are treated in the next section.

Electrons and isolated photons are reconstructed within the same Particle Flow step to account for similar behavior within the tracker bulk. There is a large probability for both a) an electron to radiate a brehmsstrahlung photon and b) for a photon to convert to an e^+e^- pair. Therefore in object reconstruction care must be taken to collect the photons radiated from electrons in order to make appropriate measurements of the particles.

(3) Hadrons & non-isolated Photons:

Hadrons & non-isolated photons result from hadronization/fragmentation of jets. ECAL clusters not associated to any tracks are assigned to be photons. Neutral hadrons (K_L^0 , neutrons) are reconstructed from HCAL clusters with no associated track; neutral hadrons leave a very small amount of energy in the ECAL. Charged hadrons (π^\pm , K^\pm , protons) are reconstructed using the remaining tracks and HCAL deposits. Charged hadrons do not radiate bremsstrahlung photons nor cause e^+e^- pair creation and thus do not leave signals in the ECAL.

(4) Nuclear Interactions:

6.3 Additional High-Level Objects

6.3.1 Jets

Bare quarks and gluons can never be observed in Nature due to a QCD phenomenon called *color confinement*. Therefore, quark and gluon production manifests as a “jet” of color-neutral particles emanating from the production point. These particles can be clustered together to reconstruct the original parton. The jets used in this analysis are made by clustering particles with the “anti-kt” algorithm with cone sizes of $\Delta R = 0.4, 0.8$ [15], denoted as AK4 and AK8 jets respectively. This algorithm produces nearly conical jets but with an added benefit of being more robust to effects of soft radiation. The AK4 jets subtend less solid angle and are used to capture the hadronisation of single quarks and gluons. AK8 jets subtend a larger solid angle and are used for reconstruction of boosted objects (e.g. t , H , Z , W).

6.3.2 b-tagging of Jets

Jets resulting from the production of b quarks (and to some extent c quarks) garner special attention in our experiment. As usual for quarks and gluons, the b-quark will quickly hadronize and form a b hadron. But what is unique about the b hadrons are the values their lifetimes take such that they can travel hundreds of μm before decaying inside our detector. Vertexing the tracks resulting from the decay will reveal the presence of a *secondary vertex* which is spatially displaced from the rest of the hadrons inside the jet. This secondary vertex allows for one handle on being able to identify jets as coming from b quark production. Other handles include the momenta and multiplicity of the other particles clustered into the jet.

In addition to tagging jets as originating from a single b quark, tagging of jets as originating from **two** b quarks is also possible.[16] As would be expected, this technique makes heavy use of the presence of **two** secondary vertices. The analysis presented in Section 7 makes extensive use of this technique.

6.3.3 Neutrinos – Invisible Particles $\rightarrow p_T^{\text{miss}}$

Neutrinos are so weakly interacting that they leave no energy deposits in CMS and therefore cannot be detected by our experiment. Although direct detection is not possible, we are still able to *infer* the presence of a neutrino. The protons involved in the initial collision have no net momentum in the transverse direction; the summed momenta of all the final state particles should therefore be equal to zero in the direction transverse to the beamline. Any non-zero value for the final-state transverse momentum is thus indicative of a neutrino escaping unscathed. We define this imbalance as

$$p_T^{\text{miss}} \equiv \left| - \sum_i \vec{p}_T \right|, \quad \forall \text{ particles i.} \quad (6.1)$$

In addition to SM neutrinos, many theories of beyond the Standard Model physics predict particles which are expected to give rise to a source of p_T^{miss} .

6.3.4 π^0 meson

Charged and neutral π mesons are the lightest of all hadrons with masses of 135 and 140 MeV, respectively. The next massive are the K mesons at 495 MeV; the lightest baryons are neutrons and protons, with masses of 940 MeV. Pions are therefore copiously produced within hadronic interactions and often contain much of the jet energy. As a rule-of-thumb, the charged to neutral energy fraction within a jet is approximately two-thirds to one-third (to match the pion and Kaon multiplicities).

Because the neutral pion branching to photons is over 98% and its lifetime is relatively short (25.5 nm), the detection of neutral pions therefore involves reconstruction of photon pairs with the appropriate invariant mass. This is simple enough in principle, but as the pion p_T increases the photons from the pion decay become more and more collimated. Eventually, for pions above about 7 GeV, individual photons are not able to be resolved because of the ECAL resolution (crystal size), the same crystal gets the energy from both photons. This was the primary motivation for the Preshower ECAL detector.

Chapter 7

Search for physics beyond the Standard Model using boosted H bosons and missing transverse momentum in proton-proton collisions at 13 TeV

7.1 Motivation & Strategy

If a more unifying theory than the SM exists it certainly has not been forthright in its manifestation. One possibility for the lack of discoveries of phenomena not explained within the SM is that there are indeed particles existing in Nature which have not been observed, but they have such a large mass the energy of the proton-proton collisions provided by the LHC is insufficient to directly create them. The outcome of many searches for new particles is thus the setting of lower limits placed on the mass – if the particle were any lighter than this limit it would have been produced copiously enough for its unambiguous detection (see for example [17], [18]). As these particles become more massive more momentum is imparted upon the particles involved in the final state; any SM particles resulting from the decay of higher mass states will be produced with large momentum (this is called high boost). As a particle becomes more boosted its decay products are emitted at smaller angles, eventually collimating sufficiently to be reconstructed as a single jet. If new physics exists with masses achievable by the LHC, one could suspect that there exists non-zero coupling with the electroweak H, Z, or W bosons. Observation of events containing high- p_T (>300 GeV) electroweak bosons are thus of considerable interest for some hints of something unseen.

The Minimal Supersymmetric SM contains a \mathbb{Z}_2 symmetry in which all SM particles have charge -1 and all supersymmetric particles have charge +1, this is called R-parity[2]. One direct

consequence of R-parity is that the decay of a massive supersymmetric particle must include at least one supersymmetric particle in the final state. Necessarily this is the lightest such particle in the theory, denoted the lightest supersymmetric particle (LSP). If the LSP is electrically neutral it may escape detection, creating an imbalance in the net momentum of the event (as would a neutrino). Events with a large momentum imbalance are also interesting as potential regions for SUSY.

With this as motivation, we designed an analysis searching for hints of new physics beyond the SM in events with boosted H or Z bosons and a large transverse momentum imbalance of the event. We reconstruct the H and Z bosons in the $b\bar{b}$ channel, with 57% and 15% branching fractions respectively. Although our analysis is sensitive to any new physics with this final state, we have adopted two benchmark models (known as SMS models[19], which are phenomenological models of SUSY production), seen in Figure 7.1, to give motivation to the analysis. In this scenario, the proton-proton interaction produces a pair of gluinos \tilde{g} which decay to a neutralino $\tilde{\chi}_2^0$ by the emission of SM quarks. A small mass splitting between the gluino \tilde{g} and neutralino $\tilde{\chi}_2^0$ will result in low- p_T SM quarks and a high- p_T neutralino $\tilde{\chi}_2^0$. This neutralino $\tilde{\chi}_2^0$ further decays into neutralino $\tilde{\chi}_1^0$ with the emission of a H or Z boson. The neutralino $\tilde{\chi}_1^0$ is the LSP and escapes detection.

Past searches targeting similar final states (but different production scenario, i.e. another SMS model) have been performed in which the H bosons are produced with low- p_T , in this case the H bosons are reconstructed as a resolved pair of b-tagged AK4 jets [20].

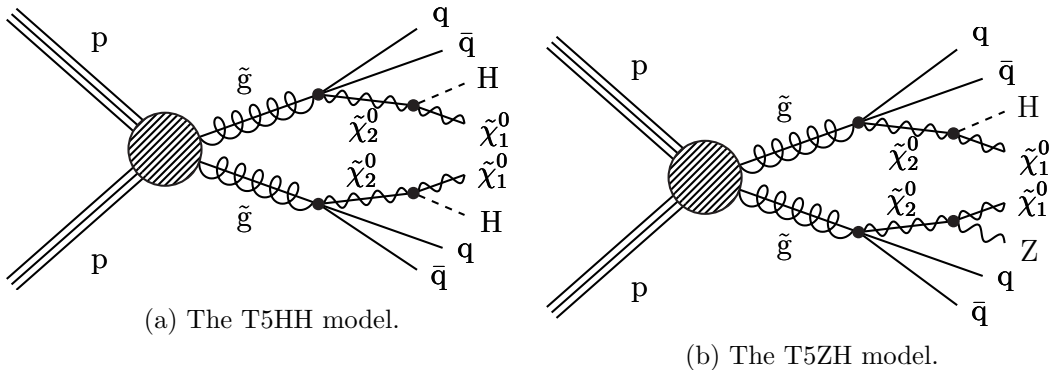


Figure 7.1: Diagrams of the benchmark models used for motivation of the targeted signal.

7.2 Object Definition & Event Selection

We establish a baseline selection choosing events with all-hadronic final states and missing transverse momentum (p_T^{miss}), as motivated by Figure 7.1. The baseline selection is as follows:

- ≥ 2 AK8 jets; $p_T > 300 \text{ GeV}$ and $50 < \text{mass} < 250 \text{ GeV}$
- $p_T^{\text{miss}} > 300 \text{ GeV};$
- isolated electron veto; $p_T > 10 \text{ GeV}$

To remove events with top or W production in which the W decays to an electron.

- isolated muon veto; $p_T > 10 \text{ GeV}$

To remove events with top or W production in which the W decays to a muon.

- isolated track veto

To remove events with top or W production in which the W decays to a tau. The tau branching fraction to states containing at least one charged particle is 85%. As an isolated track is defined by looser criteria than that of an electron or muon, this cut also serves to increase the efficiency of the isolated electron and muon vetoes.

- $\Delta\phi_{1,2,3,4} > 0.5, 0.5, 0.3, 0.3$; $\Delta\phi_i \equiv \Delta\phi(p_T^{\text{miss}}, \text{AK4 jet}_i)$

The $\Delta\phi$ cut is designed to mitigate QCD events in which a jet is under-measured leading to an artificial imbalance in the event momentum. This cut requires that the difference in ϕ between the p_T^{miss} vector and each of the four leading AK4 jets is sufficiently large to remove events in which a jet has been under-measured giving rise to fake p_T^{miss} pointing in the same direction. If less than four AK4 jets are available the additional cuts are removed.

A dedicated heavy tagging algorithm is used to identify AK8 jets arising from the decay of two b quarks [16]. The distribution of the output discriminator for the lead and sub-leading jets are seen in the left and right panels of Figure 7.2, respectively; signal-like events peak towards larger values. To $b\bar{b}$ tag the AK8 jets we choose the loose working-point (>0.3) corresponding to a signal

efficiency of approximately 80% per AK8 jet (see Section 7.8). The stacked histogram and solid lines shows the distribution after baseline selection for simulation and two representative signal points, respectively.

Further H/Z tagging of an AK8 jet is accomplished by restricting the jet mass window to [85, 135 GeV] to be consistent with that of the H boson. The distributions of the jet mass are seen in Figure 7.2. The signal shown in the solid line is the T5HH model (i.e. Figure 7.1a). The same identification criteria are applied to tag an AK8 jet as either an H or Z boson, there is no distinction made.

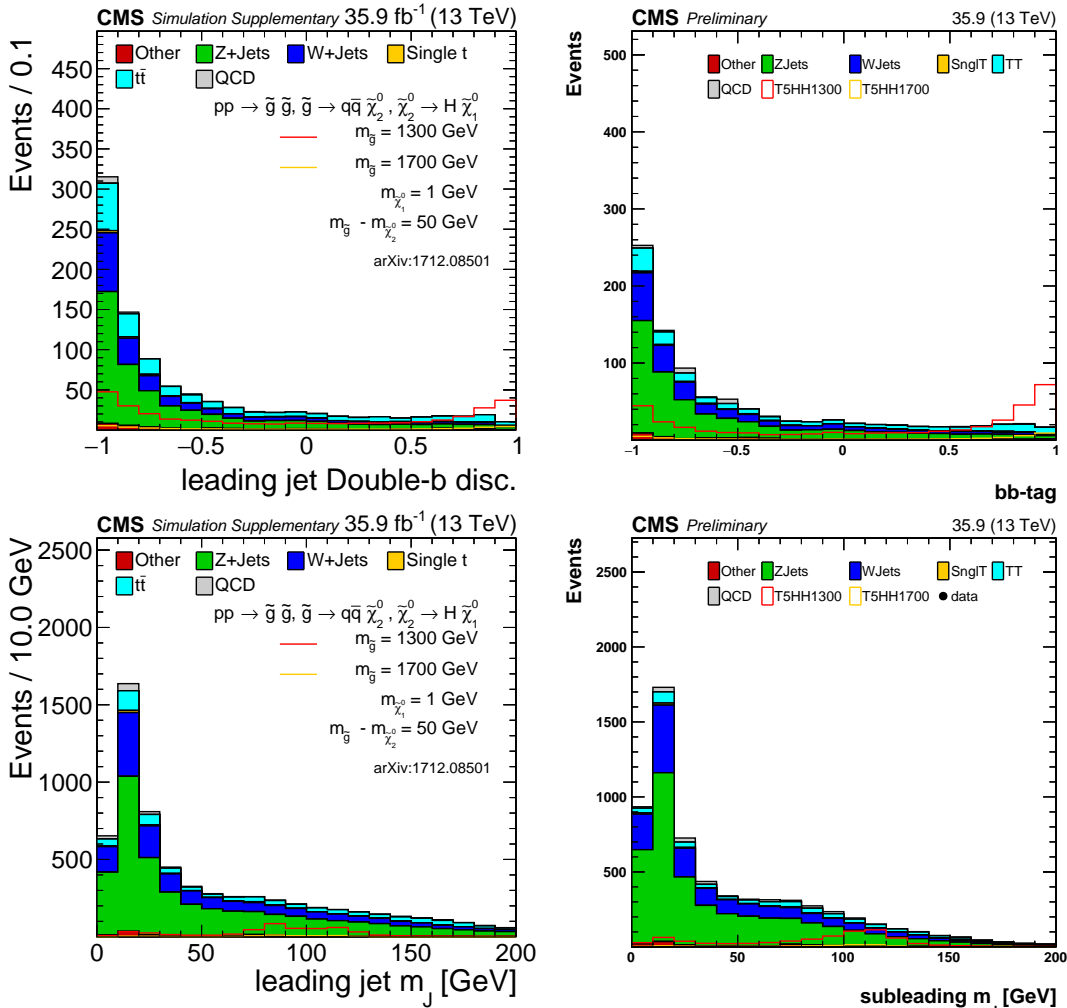


Figure 7.2: Distributions of bb-tagging discriminator (top row) and the jet mass (bottom row) for the leading (left column) and subleading (right column) AK8 jets. These are used in H/Z tagging of AK8 jets.

7.3 Dataset & Trigger

We use a total of 35.9 fb^{-1} of data collected by the CMS experiment in 2016. Events are selected in data using a trigger which requires greater than 100 GeV of p_T^{miss} calculated at high-level trigger (HLT); additionally the logical OR of two other triggers with thresholds of 110 and 120 GeV are applied. The trigger efficiency is derived in data using a single-electron reference trigger requiring a tight-ID electron of $p_T > 27 \text{ GeV}$. We further select events with at least three AK4 jets and exactly one reconstructed electron of $p_T > 25 \text{ GeV}$. The signal region trigger is found to be greater than 98% for events with $p_T^{\text{miss}} > 250 \text{ GeV}$ and $\text{HT} > 300 \text{ GeV}$ [17].

7.4 Event Simulation

Event simulation of the proton-proton collisions proceeds in a step-wise manner. To simulate the hard physics process MadGraph@NLO2.2.2 [21] is used to calculate matrix-element amplitudes. The parton distribution functions (PDFs) used in these calculations are from NNPDF 3.0 [22]. Parton showering and other event dynamics are generated with Pythia.[23] The simulation of the interaction of the final state particles with the detector is performed with GEANT [24]. This “raw” simulation data is then at the same tier as data collected from the physical experiment and is merged into a single pipeline for event reconstruction.

7.4.1 Standard Model Processes

The SM samples which enter as the primary backgrounds are listed in Table 7.1 (see Section 7.5.1 for a discussion of the SM background). All samples are generated with a pileup distribution with an average of 25 interactions per bunch crossing and a 25ns interval between bunches. For acceptable statistics over a wide range of parameter space, the MC samples are often binned in $\text{HT} \equiv \sum_{\text{AK4 jets}} p_T$. As our event selection requires at least two AK8 jets with $p_T > 300 \text{ GeV}$ we roughly operate in regime of $\text{HT} > 600 \text{ GeV}$.

Table 7.1: SM MC samples used in the analysis.

process	final state	HT (GeV)	σ (pb)	$\int \mathcal{L}$ (fb^{-1})
$t\bar{t}$	$t \rightarrow \ell\nu, \bar{t} \rightarrow 2q$	inclusive	182.72	283.90
$t\bar{t}$	$\bar{t} \rightarrow \ell\nu, t \rightarrow 2q$	inclusive	182.72	326.48
$t\bar{t}$	2ℓ	inclusive	88.34	346.25
$t\bar{t}$	inclusive	[600, 800]	2.734	5231.81
$t\bar{t}$	inclusive	[800, 1200]	1.121	9416.61
$t\bar{t}$	inclusive	[1200, 2500]	0.198	14819.34
$t\bar{t}$	inclusive	[2500, ∞]	0.002	221088.29
QCD	inclusive	[200, 300]	1735000	0.03
QCD	inclusive	[300, 500]	366800	0.16
QCD	inclusive	[500, 700]	29370	1.95
QCD	inclusive	[700, 1000]	6524	6.68
QCD	inclusive	[1000, 1500]	1064	12.62
QCD	inclusive	[1500, 2000]	121.5	32.63
QCD	inclusive	[2000, ∞]	25.42	239.30
Z+jets	$\nu\bar{\nu}$	[100, 200]	344.8	54.13
Z+jets	$\nu\bar{\nu}$	[200, 400]	95.53	208.46
Z+jets	$\nu\bar{\nu}$	[400, 600]	13.20	77.30
Z+jets	$\nu\bar{\nu}$	[600, 800]	3.148	1795.26
Z+jets	$\nu\bar{\nu}$	[800, 1200]	1.451	1486.09
Z+jets	$\nu\bar{\nu}$	[1200, 2500]	0.355	1029.81
Z+jets	$\nu\bar{\nu}$	[2500, ∞]	0.0085	47498.87
W+jets	$\ell\nu$	[100, 200]	1627.45	18.16
W+jets	$\ell\nu$	[200, 400]	435.24	45.88
W+jets	$\ell\nu$	[400, 600]	59.18	123.64
W+jets	$\ell\nu$	[600, 800]	14.58	221.32
W+jets	$\ell\nu$	[800, 1200]	6.66	1123.13
W+jets	$\ell\nu$	[1200, 2500]	1.608	153.44
W+jets	$\ell\nu$	[2500, ∞]	0.039	6497.28

7.4.2 Signal Models

For commissioning of the analysis technique (as well as the limit-setting procedure, see Section 7.7) Monte Carlo samples with our final-state signal topology were generated, as in Figure 7.1. The signal sample follows the same processing chain as the SM samples. The mass splitting between the gluino \tilde{g} and neutralino $\tilde{\chi}_2^0$ is fixed to 50 GeV, resulting in low p_T SM quarks produced in the gluino \tilde{g} decays. The mass of the neutralino $\tilde{\chi}_1^0$ (LSP) is fixed to 1 GeV. We have samples with a range of gluino \tilde{g} masses from 750 to 2200 GeV. The p_T distribution for the generated H bosons in these samples is seen in Figure 7.3 for a number of gluino \tilde{g} masses. Additionally the angular separation $\Delta R \equiv \sqrt{\Delta\phi^2 + \Delta\eta^2}$ between the $b\bar{b}$ pair is shown. As the p_T of a parent boson increases the $b\bar{b}$ pair from its decay tend to align, allowing complete reconstruction with a single AK8 jet.

7.5 Event Binning & Background Estimation

The background estimation procedure makes use of what is known as an “ABCD” prediction in which the analysis phase space is divided into signal and sideband regions; scaling relations are applied to sideband yields to make predictions for the SM background (inclusive in all processes) in the signal regions. The events are categorized according to whether the two leading AK8 jets are a) in the signal or sideband mass region and b) have or have not been $b\bar{b}$ tagged. A diagram of this partitioning is seen in Figure 7.4. An additional dimension is added by binning in p_T^{miss} : [300, 500 GeV], [500, 700 GeV], [700, ∞ GeV]. This gives a total of $2 \times 3 = 6$ signal and $4 \times 3 = 12$ sideband bins. The two signal regions $A_{1,2}$ contain events with one (and only one) or two jets being consistent with H/Z boson decay, respectively.

Assuming that there is no correlation between the jet mass and the $b\bar{b}$ tagging one would expect that

$$\frac{A_{1,2}}{B_{1,2}} = \frac{C}{D} \quad (7.1)$$

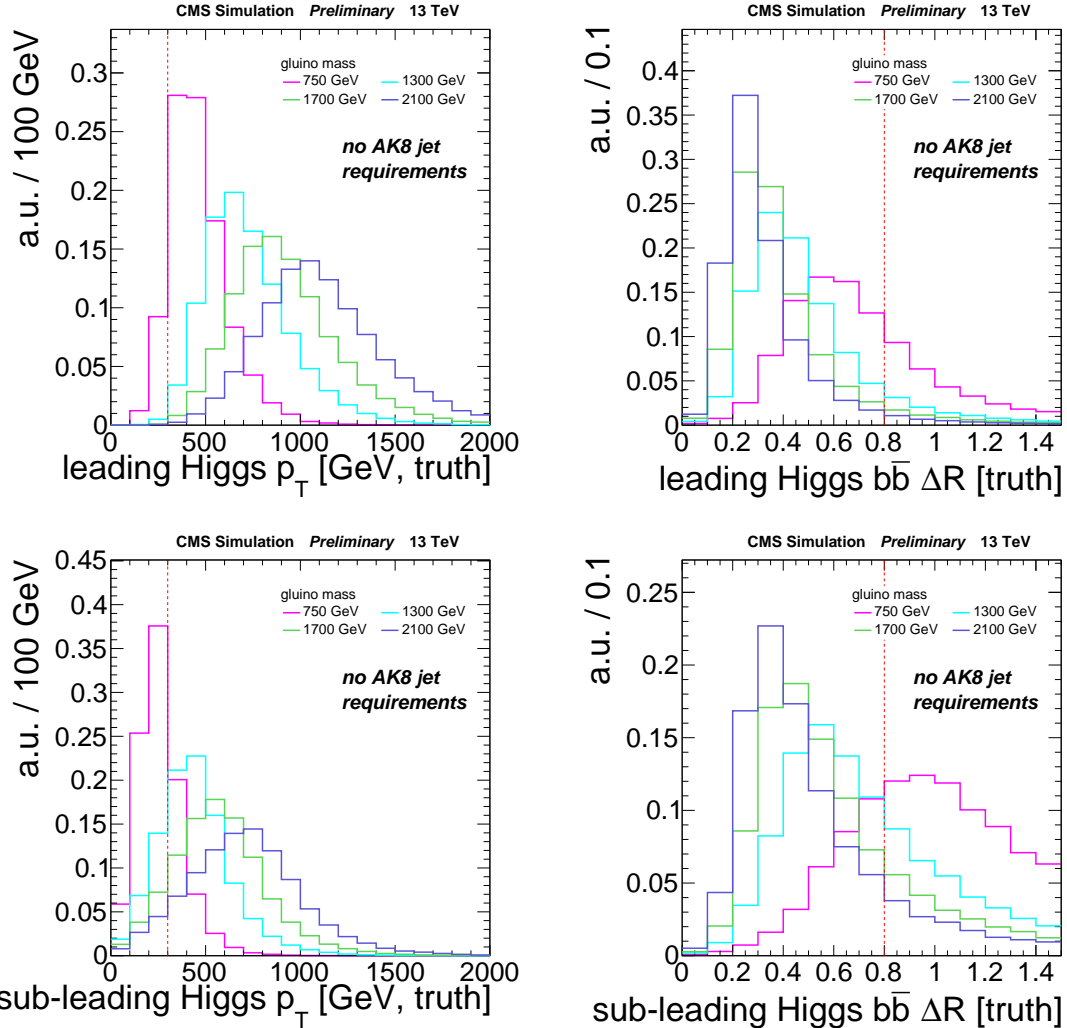


Figure 7.3: Generator level distributions for the leading (top row) and subleading (bottom row) H boson in the T5HH model. The plot on the left shows the p_T of the H boson. The plot on right shows ΔR between the b-quark daughters - for large H p_T the daughters become collimated.

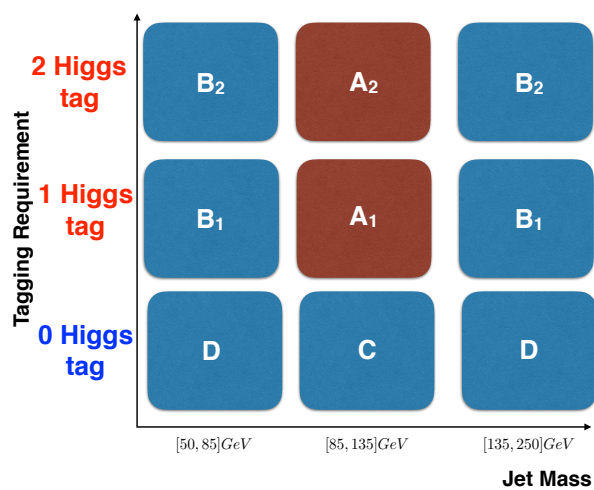


Figure 7.4: A diagram of the partitioned phase space. p_T^{miss} binning brings the number of bins to $6 \times 3 = 18$.

Rearranging this gives a prediction for the events in the signal regions

$$A_{1,2}^{\text{predicted}} = (B_{1,2} \cdot \frac{C}{D})^{\text{observed}} \quad (7.2)$$

The expected p_T^{miss} distribution from simulation is seen in the stacked histograms of Figure 7.5. The prediction using the ABCD method is seen in the red hash. The expected level of closure in simulation can be determined by dividing the true content in the signal region with the prediction. This ratio, denoted κ , is seen in the bottom panel of Figure 7.5. $\kappa = 1$ represents perfect closure. As will be discussed in Section 7.5.2, κ is used as a correction in the background estimation procedure.

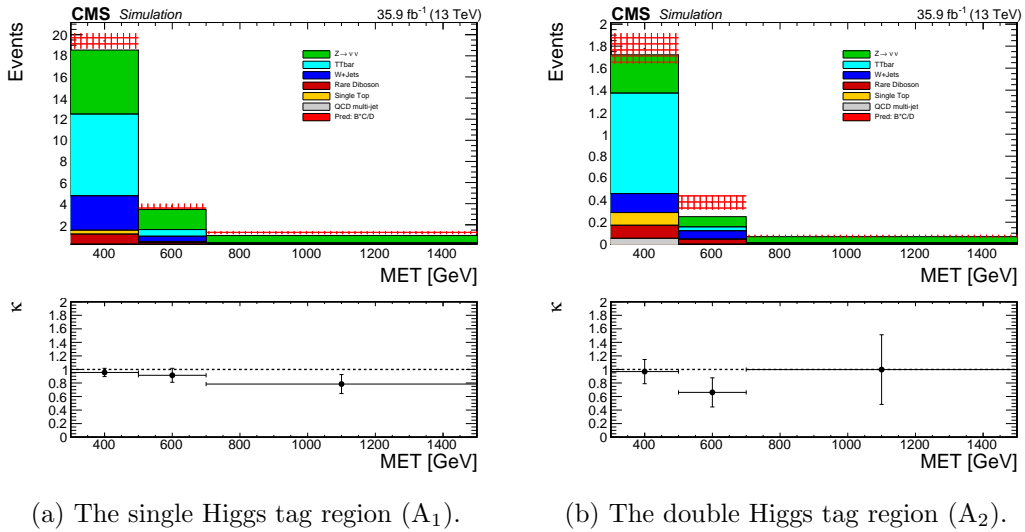


Figure 7.5: p_T^{miss} distributions and predictions in the signal regions using simulation only.

7.5.1 Control Regions within Data

We treat the SM backgrounds in the analysis as consisting of three main components (hinted at the list of MC samples seen in Table 7.1):

- $Z \rightarrow \nu\bar{\nu}$ in which the invisible Z gives true p_T^{miss} ('Z-invisible').
- Semi-leptonic W or t production in which the lepton is not identified, the associated neutrino from the leptonic decay creates true p_T^{miss} ('lost-lepton').

- Jet production via QCD in which the p_T of a jet is substantially under-measured, this creates a fake source of p_T^{miss} .

Three control regions are defined to serve as a proxy for each source. They are defined with the same event selection as the signal and control regions, with the exception of the inversion of a single cut.

- A control region with a single-photon, after artificially removing the photon from event reconstruction, closely mimics the Z-invisible background. For high- p_T , both photons and Z bosons become massless, neutral, gauge bosons whose kinematics are expected to be similar.
- A control region with a single-lepton, mimics the lost-lepton background.
- A control region defined by the logical inversion of the low- $\Delta\phi$ cuts, most closely mimics the QCD background. This enriches our events with those likely in which p_T^{miss} is aligned with an under-measured AK4 jet.

As they are orthogonal to the analysis region, we are able to test the closure of the background estimation technique independently within each of the three control regions. By comparing the prediction of the SM yields (using the ABCD method) with those observed, the validity of the technique can be verified for that particular background category. The comparisons for the single-photon, single-lepton and low- $\Delta\phi$ control regions can be seen in Figure 7.6. κ in the bottom panel is defined as the ratio of the true event yield to the prediction. $\kappa = 1$ represents the case of perfect closure. These comparisons are used for commissioning of the background estimation technique only.

7.5.2 κ as a Correction to the Estimation

To correct for the observed non-closure of the background estimation method a correction κ is applied to the SM background prediction. κ is obtained by dividing the MC yields for the signal

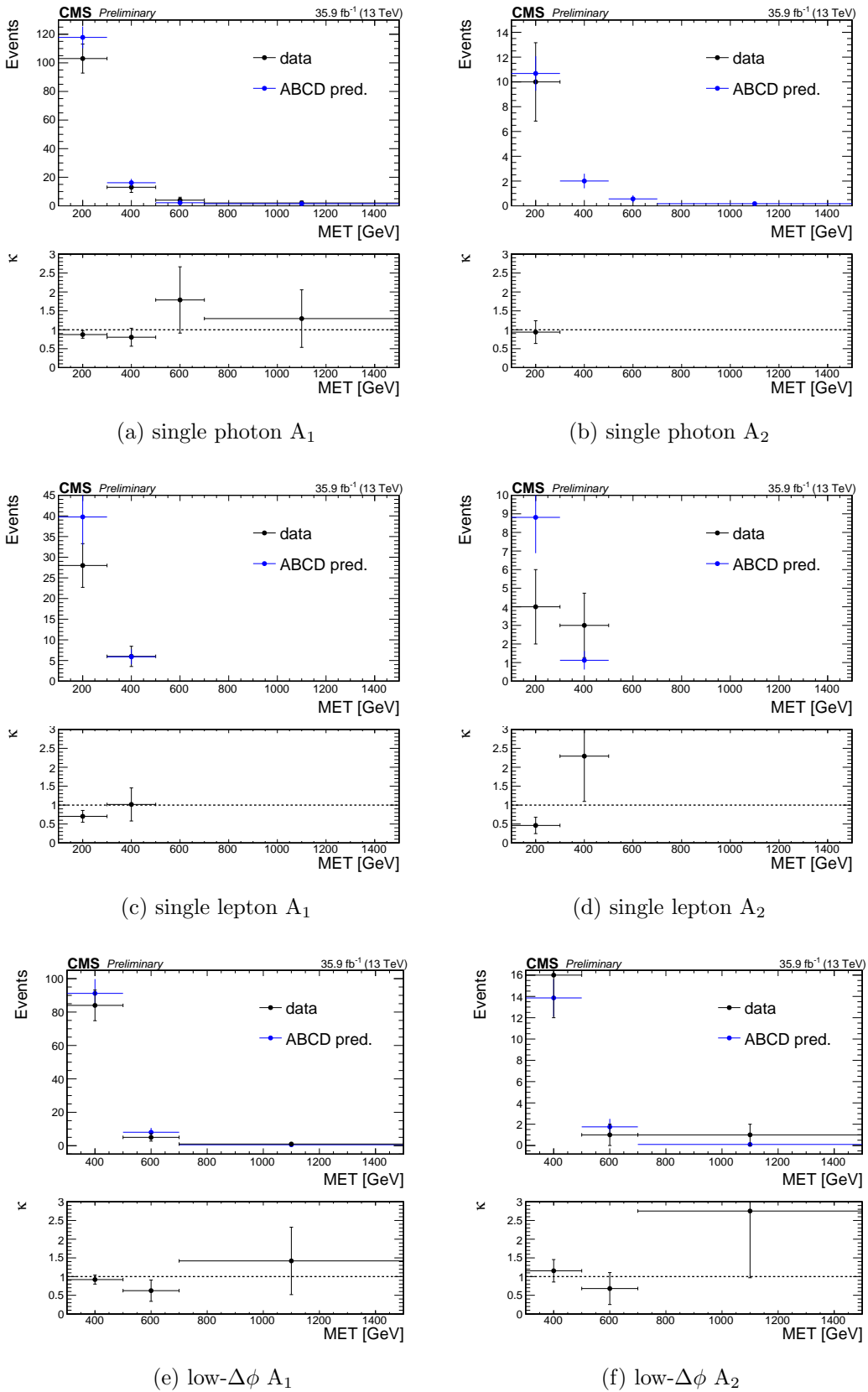


Figure 7.6: Closure observed within the data control regions.

region by that predicted:

$$\kappa \equiv A^{mc} / \left(B \cdot \frac{C}{D} \right)^{mc} \quad (7.3)$$

There are $2 \times 3 = 6$ values of κ , one for each signal bin. $\kappa = 1$ represents the case of perfect closure. The corrections are then applied as follows:

$$A_{1,2}^{\text{predicted}} = \kappa \cdot \left(B_{1,2} \cdot \frac{C}{D} \right)^{\text{observed}} \quad (7.4)$$

These values of κ are those which we have already seen in Figure 7.5.

The value of κ is dependent on the yields of each analysis bin and is therefore sensitive to the accuracy of the modeling of MC in each of the 18 analysis bins. To improve the determination of κ , scale factors are derived using the data control regions to correct the normalization of MC in each of these bins. Different scale factors are assigned separately to the Z-invisible, lost-lepton, and QCD background MC samples. Rare processes (e.g. diboson) are taken directly from MC.

First consider how the yield N predicted by MC in an arbitrary bin (of 18) is the sum of the yields in the different MC datasets ($t\bar{t}$ and $W \rightarrow \ell\nu$ are grouped as they together represent the lost-lepton background):

$$N^{mc} = N_{Z \rightarrow \nu\bar{\nu}}^{mc} + N_{t\bar{t}, W \rightarrow \ell\nu}^{mc} + N_{QCD}^{mc} + N_{rare} \quad (7.5)$$

Scale factors are defined for this bin using the corresponding control regions in data and forming the ratio of events in simulation to that observed. They are then applied as follows:

$$N_{\text{corrected}}^{mc} = \left(\frac{N_{\text{single}-\gamma}^{\text{data}}}{N_{\text{single}-\gamma}^{mc}} \right) \cdot N_{Z \rightarrow \nu\bar{\nu}}^{mc} + \left(\frac{N_{\text{single}-\ell}^{\text{data}}}{N_{\text{single}-\ell}^{mc}} \right) \cdot N_{t\bar{t}, W \rightarrow \ell\nu}^{mc} + \left(\frac{N_{\text{low}-\Delta\phi}^{\text{data}}}{N_{\text{low}-\Delta\phi}^{mc}} \right) \cdot N_{QCD}^{mc} + N_{rare} \quad (7.6)$$

The p_T^{miss} distribution within the control regions is shown for both data and MC in Figures 7.7, 7.8, 7.9 for the single photon, single lepton, and low- $\Delta\phi$ control regions, respectively. The ratio in the bottom panel of each plot represents the scale factor for that p_T^{miss} bin. The dotted

horizontal line shows the average scale factor inclusive in p_T^{miss} . The scale factors for the single-photon and low- $\Delta\phi$ control regions show no p_T^{miss} dependence and are determined integrated over $p_T^{\text{miss}} > 300 \text{ GeV}$. The values of the scale factors are summarized in Table 7.2. The Single-lepton region, shown in Figure 7.8, does show p_T^{miss} dependence and are summarized in Tables 7.2 and 7.3. In order to improve statistics for the single-lepton region, the low- $\Delta\phi$ requirement has been removed.

Table 7.2: Summary of the control region scale-factors integrated over p_T^{miss} .

Low $\Delta\phi$					
A_{SF}^{1H}	A_{SF}^{2H}	C_{SF}	B_{SF}^1	B_{SF}^2	D_{SF}
1.1 ± 0.33	0.85 ± 0.12	0.93 ± 0.1	0.88 ± 0.04	1.2 ± 0.16	0.71 ± 0.027
Single Lepton					
A_{SF}^{1H}	A_{SF}^{2H}	C_{SF}	B_{SF}^1	B_{SF}^2	D_{SF}
0.61 ± 0.04	0.59 ± 0.08	p_T^{miss} dependent	0.59 ± 0.016	0.71 ± 0.04	p_T^{miss} dependent
Photon					
A_{SF}^{1H}	A_{SF}^{2H}	C_{SF}	B_{SF}^1	B_{SF}^2	D_{SF}
0.61 ± 0.088	0.75 ± 0.29	0.5 ± 0.07	0.98 ± 0.094	2.58 ± 0.63	0.71 ± 0.035

Table 7.3: Summary of the Single Lepton control region scale-factors in the anti-tag sideband region.

Single Lepton C_{SF}		
p_T^{miss} [300, 500]	[500, 700]	[700, ∞]
0.47 ± 0.05	0.54 ± 0.15	0.18 ± 0.1
Single Lepton D_{SF}		
0.49 ± 0.02	0.40 ± 0.05	0.35 ± 0.08

The scale factors are then applied to the MC samples to give yields which better reflect data. The p_T^{miss} distributions for the signal regions and expectations from the ABCD background prediction are seen in Figure 7.10 (the data-corrected version of Figure 7.5). The improved value of κ is seen in the lower panel of each plot. The modified values of the MC yields in the signal region (seen in the calculation of κ) are seen in Tables 7.5 and 7.6. Since most of the scale factors are less than one the background decreases in Figure 7.5 relative to Figure 7.10 but still preserves closure so that κ is statistically compatible with unity. A distribution of κ is derived by throwing

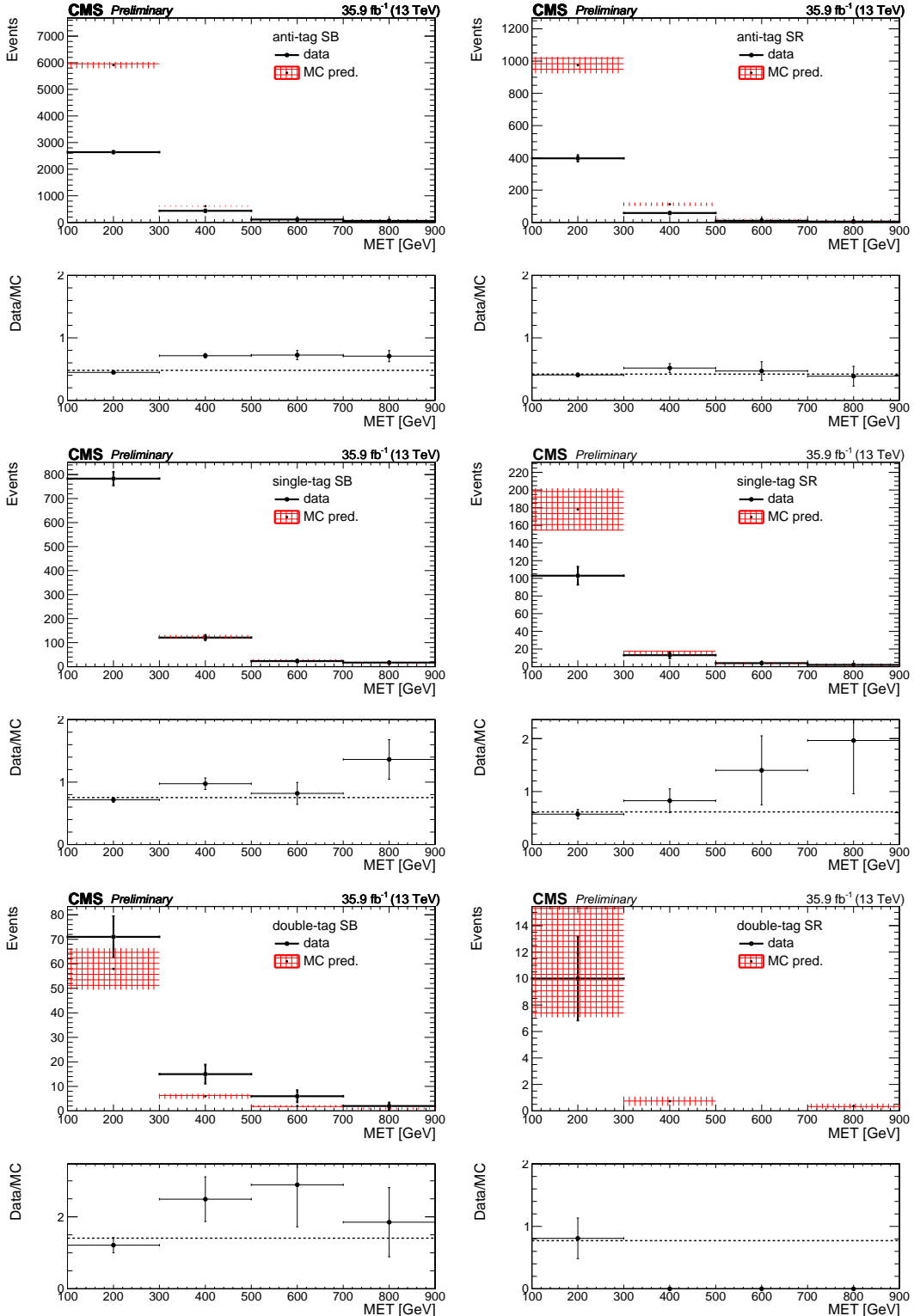


Figure 7.7: Signal and sideband yields in the single photon control region. The hashed red band denotes the prediction from simulation; the solid black points denote the observed yields in data. The Data/MC ratio in the lower panel of each plot represents the scale factor for that bin.

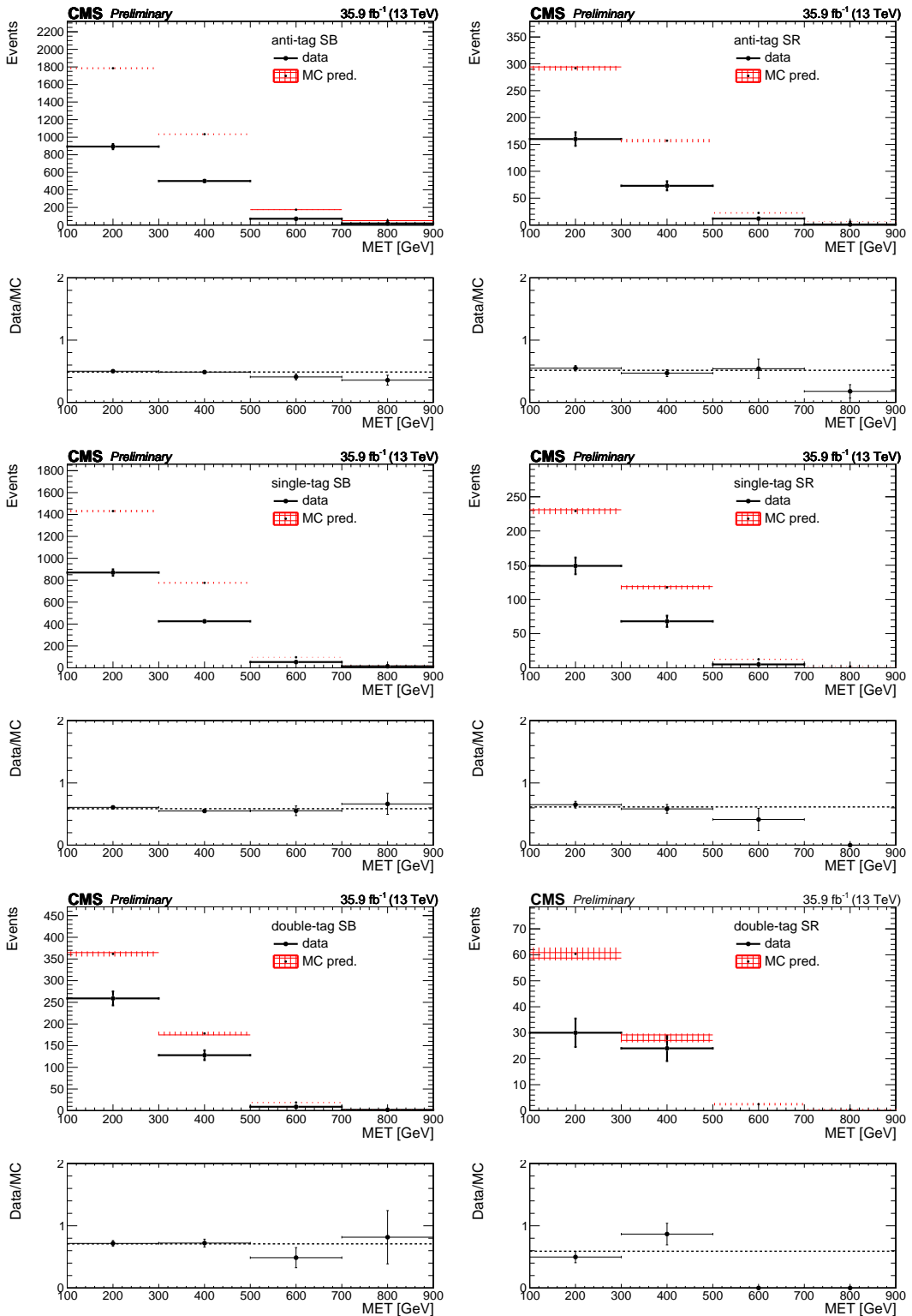


Figure 7.8: Signal and sideband p_T^{miss} yields in the single lepton control region. The hashed red band denotes the prediction from simulation; the solid black points denote the observed yields in data. The Data/MC ratio in the lower panel of each plot represents the scale factor for that bin. The low- $\Delta\phi$ requirement has been removed to improve statistics.

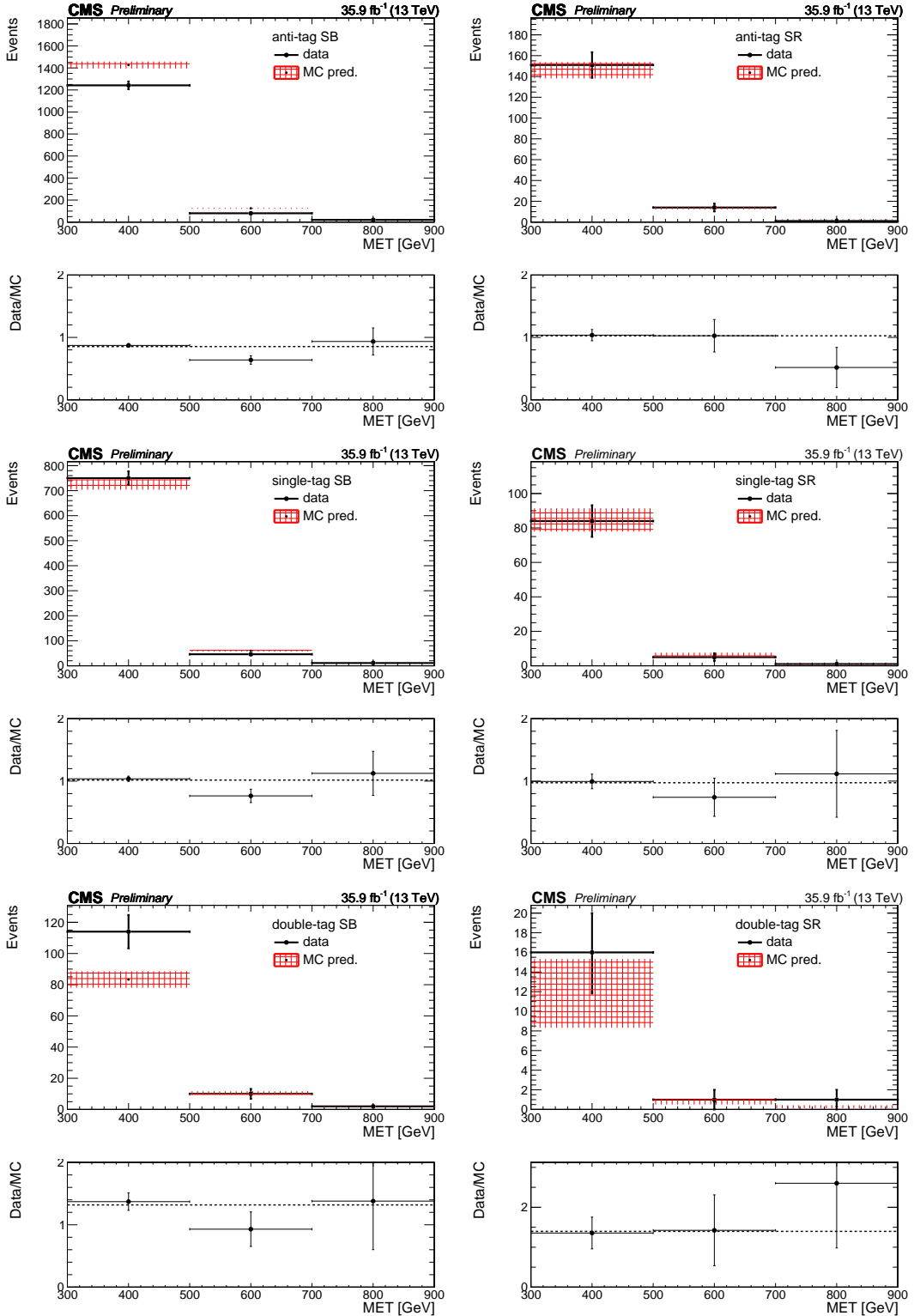
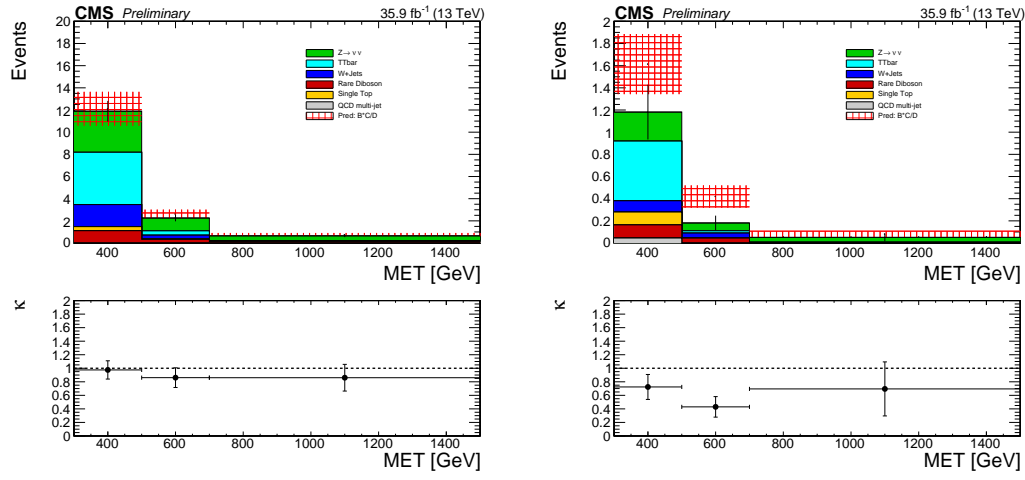


Figure 7.9: Signal and sideband p_T^{miss} yields in the low- $\Delta\phi$ control region. The hashed red band denotes the prediction from simulation; the solid black points denote the observed yields in data. The Data/MC ratio in the lower panel of each plot represents the scale factor for that bin.

gaussian toys for each of the scale factors, the final results being summarized in Table 7.4.

Table 7.4: The κ factor computed by throwing Gaussian toys for the scale factors.

	1-Higgs Tag	2-Higgs Tag
	κ	
p_T^{miss} [300, 500 GeV]	0.98 ± 0.11	0.73 ± 0.14
p_T^{miss} [500, 700 GeV]	0.86 ± 0.16	0.43 ± 0.12
p_T^{miss} [700, ∞ GeV]	0.86 ± 0.17	0.62 ± 0.30



(a) The single Higgs tag region (A_1).

(b) The double Higgs tag region (A_2).

Figure 7.10: p_T^{miss} distributions and the predictions in the signal regions using simulation with scale factors from data.

Table 7.5: Corrected MC Yields in the signal regions.

p_T^{miss}	Z+Jets	W+Jets	T#bar{T}bar	QCD	Rare	Total	Data
Region: A^{1H}							
[300, 500] GeV	3.76 ± 0.54	2.05 ± 0.30	4.87 ± 0.72	0 ± 0	1.48 ± 0.40	12.17 ± 1.03	15
[500, 700] GeV	1.18 ± 0.21	0.33 ± 0.08	0.40 ± 0.12	0 ± 0	0.39 ± 0.16	2.30 ± 0.29	2
> 700 GeV	0.43 ± 0.10	0.053 ± 0.025	0.046 ± 0.01	0 ± 0	0.13 ± 0.053	0.66 ± 0.12	1
Region: A^{2H}							
[300, 500] GeV	0.26 ± 0.12	0.11 ± 0.05	0.58 ± 0.21	0.045 ± 0.05	0.23 ± 0.12	1.24 ± 0.28	1
[500, 700] GeV	0.07 ± 0.045	0.049 ± 0.031	0.022 ± 0.0098	0 ± 0	0.045 ± 0.039	0.19 ± 0.068	0
> 700 GeV	0.044 ± 0.032	0.005 ± 0.005	0 ± 0	0 ± 0	0.002 ± 0.016	0.051 ± 0.036	0

Table 7.6: Corrected MC Yields in each of the signal and sideband regions.

p_T^{miss}	Z+Jets	W+Jets	T#bar{T}bar	QCD	Rare	Total	Data
Region: C							
[300, 500] GeV	17.66 ± 2.52	8.23 ± 1.44	3.87 ± 0.73	0.81 ± 0.49	2.78 ± 1.142	33.36 ± 3.24	44
[500, 700] GeV	5.20 ± 0.77	0.57 ± 0.27	0.22 ± 0.11	0 ± 0	0.63 ± 0.16	6.63 ± 0.84	12
> 700 GeV	2.48 ± 0.39	0.12 ± 0.12	0.028 ± 0.031	0 ± 0	0.14 ± 0.06	2.76 ± 0.41	4
Region: B^{1H}							
[300, 500] GeV	42.13 ± 4.17	15.61 ± 10.15	30.99 ± 20.15	1.57 ± 0.54	12.16 ± 1.37	102.47 ± 23.00	112
[500, 700] GeV	12.05 ± 1.28	2.74 ± 1.79	3.04 ± 2.00	0 ± 0	2.55 ± 0.43	20.37 ± 3.00	20
> 700 GeV	5.92 ± 0.69	0.67 ± 0.61	0.49 ± 0.46	0 ± 0	1.93 ± 0.72	9.01 ± 1.25	5
Region: B^{2H}							
[300, 500] GeV	5.51 ± 1.47	0.73 ± 0.44	4.46 ± 2.65	0.33 ± 0.23	2.06 ± 0.32	13.09 ± 3.09	13
[500, 700] GeV	1.80 ± 0.56	0.17 ± 0.11	0.59 ± 0.39	0 ± 0	0.62 ± 0.23	3.17 ± 0.73	1
> 700 GeV	0.67 ± 0.27	0.0084 ± 0.009	0.035 ± 0.031	0 ± 0	0.23 ± 0.073	0.94 ± 0.28	1
Region: D							
[300, 500] GeV	164.82 ± 8.31	61.24 ± 3.70	33.20 ± 2.16	8.50 ± 2.73	20.64 ± 1.78	288.41 ± 9.90	273
[500, 700] GeV	47.37 ± 2.52	6.36 ± 1.39	2.37 ± 0.55	0 ± 0	4.42 ± 1.46	60.51 ± 3.27	60
> 700 GeV	26.79 ± 1.50	0.99 ± 0.53	0.16 ± 0.086	0 ± 0	3.48 ± 1.01	31.42 ± 1.88	28

7.5.3 Sideband Yields & Predictions

Observed yields in data and the MC expectation for the 12 sideband bins (e.g. $B_{1,2}$, C, D in Figure 7.4) are seen in Figure 7.11. Table 7.7 lists these observed yields and calculated background prediction for the 6 signal bins.

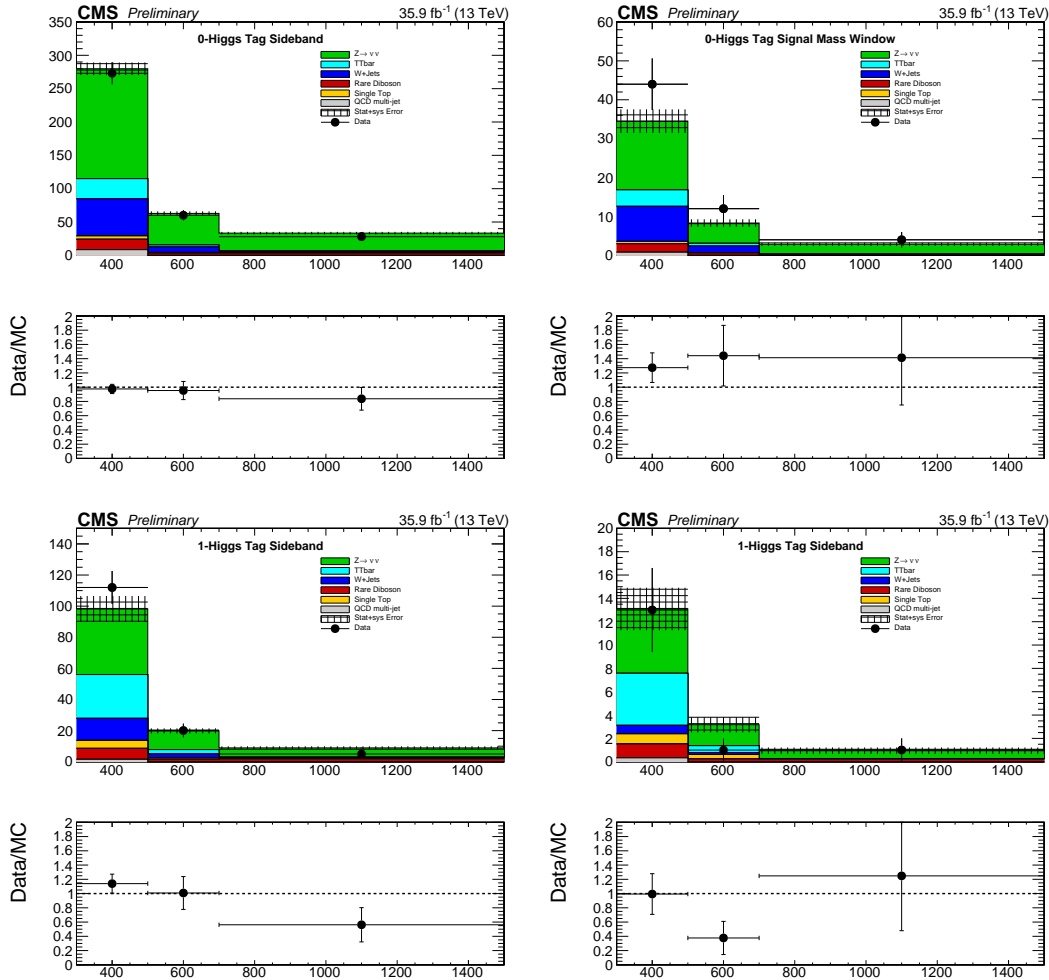


Figure 7.11: p_T^{miss} distribution in each of the control regions comparing data and the scale-factor corrected simulation. The hashed red distribution denote the prediction from simulation; the solid points denote the observed yields in data.

7.6 Signal Systematics

We consider a variety of systematic uncertainties on the signal efficiency and distribution. Some are common to more inclusive SUSY analyses [25] and there are additional systematics related to $b\bar{b}$ tagging efficiency and the effect of the pruned mass scale and resolution on the signal efficiency.

- **Luminosity:** The recommendation for the 2016 dataset is currently a flat uncertainty of 2.5%.
- **Isolated track veto:** A flat uncertainty of 2% is assigned to the signal samples to account for any data/MC differences based on the study from the 2015 analysis [25].
- **MC statistics:** The signal MC sample statistical uncertainty is generally 2-4% .
- **Trigger efficiency:** The effect of the uncertainty on the signal yield is about 2%.
- **Pileup reweighting:** The sensitivity to the pileup distribution was studied for various benchmark signal models by comparing events with $n_{\text{vtx}} < 20$ (low PU) or $n_{\text{vtx}} \geq 20$ (high PU). Accordingly, no pileup reweighting is applied to the signal MC samples and no associated uncertainty is assessed.
- **ISR:** An ISR correction is derived from $t\bar{t}$ events, with a selection requiring two leptons (electrons or muons) and two b-tagged jets, implying that any other jets in the event arise from ISR. The correction factors are 1.000, 0.920, 0.821, 0.715, 0.662, 0.561, 0.511 for NISR

Table 7.7: Observed yields in the sideband regions, κ , and background predictions for the 6 signal bins.

N_H	p_T^{miss} (GeV)	B	C	D	κ	$\kappa \cdot B \cdot C/D$
A_1	[300, 500 GeV]	112	44	273	0.98 ± 0.11	17.7 ± 3.8
A_1	[500, 700 GeV]	20	12	60	0.86 ± 0.16	3.4 ± 1.5
A_1	[700, ∞ GeV]	5	4	28	0.86 ± 0.17	0.61 ± 0.45
A_2	[300, 500 GeV]	13	44	273	0.73 ± 0.14	1.52 ± 0.57
A_2	[500, 700 GeV]	1	12	60	0.43 ± 0.12	0.09 ± 0.08
A_2	[700, ∞ GeV]	1	4	28	0.62 ± 0.30	$0.09^{+0.11}_{-0.09}$

$= 0, 1, 2, 3, 4, 5, 6+$. The corrections are applied to the simulated signal jet samples with an additional normalization factor, typically 1.15 (depending on the signal model), to ensure the overall cross section of the sample remains constant. The systematic uncertainty in these corrections is chosen to be half of the deviation from unity for each correction factor. The effect on the yield ranges from 0.01%, with the largest effect at high MET.

- **Scales:** The uncertainty is calculated using the envelope of the weights from varying the renormalization and factorization scales, μ_R and μ_F , by a factor of 2 [26, 27]. The effect on the yield of is less than 0.1%.
- **Jet Energy Corrections:** The jet energy corrections (JECs) are varied using the p_T - and η -dependent jet energy scale uncertainties from the official database. These variations are propagated into the various jet-dependent variables, including: HT, MET, $\Delta\phi(\text{MET}, j_i)$. The overall effect is less than 1%.
- **Jet Energy Resolution:** The jet momenta in the MC samples are smeared to match the jet energy resolution in data. The smearing factors are varied according to the uncertainties on the jet energy resolution measurements. These variations are propagated into the various jet-dependent variables, including: HT, MET, $\Delta\phi(\text{MET}, j_i)$. The overall effect ranges from 0.01%.
- **PDFs:** The LHC4PDF prescription for the uncertainty on the total cross section is included as ± 1 sigma bands in the results plots. No additional uncertainty is considered for the uncertainty in the acceptance due to PDFs, as per SUSY group recommendation.

The above signal systematics are applied as an uncertainty on the signal normalization. These uncertainties are in general small. The main signal systematics come from the AK8 Jet Double-b tagging efficiency data/MC scale factors and the uncertainty on the pruned mass resolution. The AK8 Jet Double-b tagging efficiency has an uncertainty which is propagated to the signal efficiency. This uncertainty is applied as a shape uncertainty across the Higgs tag regions and the anti-tag re-

gion. Also the pruned jet mass scale and resolution uncertainties are propagated to the final signal efficiency using POG recommendations. The pruned mass scale factor is derived using W-jets in semi-leptonic $t\bar{t}$ and extrapolating to the H mass. This uncertainty is assigned a shape uncertainty on the signal mass window and the sideband.

- A data/MC scale-factor is derived from double-muon tag data selected with HLT Trigger `HLT_BTagMu_AK8Jet300_Mu5_v` and muon enriched QCD Monte-Carlo. The scale factors have mainly a statistical error along with a smaller set of systematic errors due to shape systematics, Jet-Energy scale uncertainty, Pile-up corrections, uncertainty on the number of tracks, uncertainty of b-fragmentation and c-fragmentation, and the uncertainty on K_s and Λ fraction.
- The pruned mass scale-factor is derived by comparing the efficiency to select W-jets in data and MC within a mass window of [65, 85] GeV. The fit for the gaussian resolution of the W-mass peak is shown in Figure 7.12 and the fit results are shown in Table 7.8. The mass scale between MC and data is consistent though MC predicts a narrower mass resolution compared to data. The jet mass in each event is smeared to mimic the pruned jet mass resolution in data and an uncertainty is assigned based on the ratio of efficiencies between the smeared and un-smeared cases. [28]

The summary of the signal systematics and their effect on the signal yields is shown in Table 7.9. The dominant effect is from the mass resolution uncertainty.

Data	
Mean	78.2 ± 0.46
Sigma	10.10 ± 0.671
$t\bar{t}$ MC	
Mean	78.4 ± 0.35
Sigma	7.23 ± 0.48

Table 7.8: Fit results for W-mass resolution in data and MC

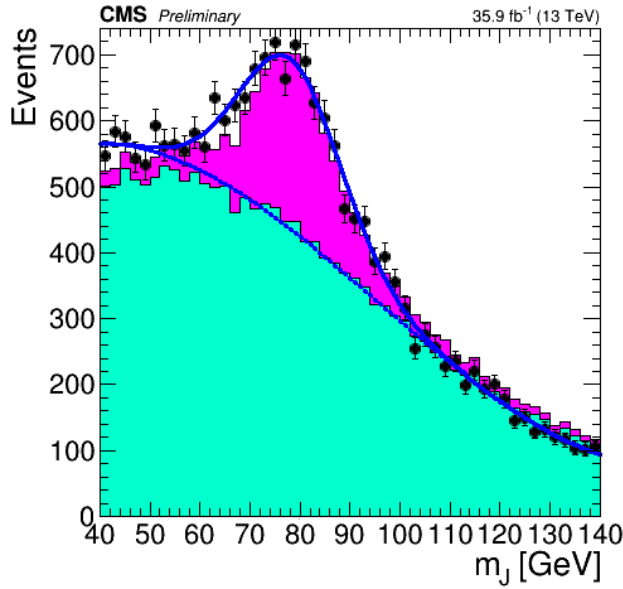


Figure 7.12: Pruned jet mass in semi-leptonic $t\bar{t}$ events. The mass peak for the W-jets is used to derive the mass resolution uncertainty.

Unc. on Normalization	
Systematic	% Effect on yields
Luminosity	2.6%
Trigger Eff.	2.0%
Iso. Track Veto	2%
ISR modeling	0.01%
PDF Scale	0.1%
JEC	1%
JER	0.01%
MC Stat	1-4%
Shape Unc.	
Double-b SF	6%
Mass Resolution	1-15%

Table 7.9: Summary of signal shape and normalization uncertainties.

7.7 Results - Yields in the Signal Regions & Exclusion Curves

After unblinding the 4x3=12 sideband regions and performing the background estimation the 2x3=6 signal regions were unblinded. The observed yields, along with the SM background predictions, are seen in Table 7.10. Our signal region yields are consistent with the SM background expectation. Additionally, Table 7.10 shows the expected signal yields for two model points corresponding to gluino \tilde{g} masses of 2000 or 1800 GeV; the mass of the neutralino $\tilde{\chi}_1^0$ is fixed at 1 GeV; the mass splitting between the gluino \tilde{g} and neutralino $\tilde{\chi}_2^0$ is fixed at 50 GeV.

Table 7.10: Signal yields and SM background predictions

p_T^{miss}	$B \cdot C/D$	κ	$\kappa \cdot B \cdot C/D$	Obs.	T5HH(2000)	T5HZ(1800)
1-Higgs Tag						
[300, 500 GeV]	18.05 ± 3.39	0.98 ± 0.11	17.68 ± 3.85	15	0.24	0.75
[500, 700 GeV]	4 ± 1.54	0.86 ± 0.16	3.44 ± 1.47	2	0.32	0.98
[700, ∞ GeV]	0.71 ± 0.50	0.86 ± 0.17	0.61 ± 0.45	1	2.13	4.34
2-Higgs Tag						
[300, 500 GeV]	2.09 ± 0.67	0.73 ± 0.14	1.52 ± 0.57	1	0.17	0.35
[500, 700 GeV]	0.2 ± 0.20	0.43 ± 0.12	$0.09^{+0.08}_{-0.08}$	0	0.23	0.44
[700, ∞ GeV]	0.14 ± 0.16	0.62 ± 0.30	$0.09^{+0.11}_{-0.09}$	0	1.36	1.98

A visual representation of the one event in the double-H tagged signal bin is seen in Figure 7.13. The purple line represents $p_T^{\text{miss}} = 426$ GeV. The three yellow cones represent the AK8 jets labeled with p_T . Note the two additional objects not satisfying our object definition but still plotted in the representation a) the additional low- p_T and low mass AK8 jet b) the $p_T=18$ GeV muon (red line) suffers from poor reconstruction properties. This event is interpreted as follows: ???.

Interpreting our results in the context of the T5HH or T5ZH models, the absence of signal allows us to place lower limits on the mass of the gluino \tilde{g} . For the statistical treatment, we use the Higgs combination tool to encode the ABCD approach in the likelihood. In this approach, the data card for one search bin contains the observed number of events and the expected signal and background in each of the ABCD regions. A likelihood function is built that contains these ABCD regions and explicitly encodes the relation $A = \kappa B \frac{C}{D}$ and a Gaussian nuisance is assigned for the

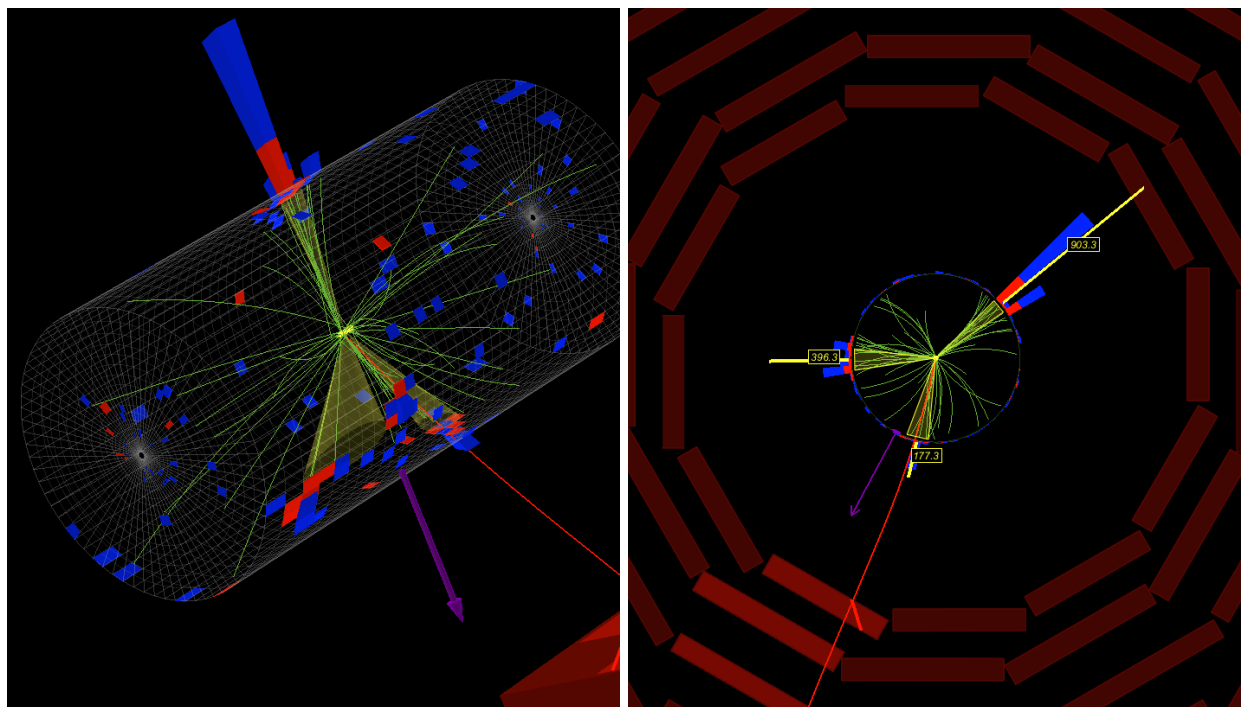


Figure 7.13: The single event in the A_2 region.

uncertainty on κ . The likelihood for each search bin can be described by:

$$\mathcal{L} = \prod_i^{ABCD} \text{Poisson}(n_i | bkg_i + r \cdot sig_i) \times \prod_j^{\text{nuisances}} \text{Constraints}(\theta_j, \hat{\theta}_j) \quad (7.7)$$

where the 4 regions are modeled by Poisson distribution and the term Constraints refers to either Gaussian distributions for the κ uncertainties or log normal distributions that model the signal systematics. The expected and observed limits are then calculated based on the asymptotic approximation of the profile likelihood ratio using the CLs criterion to place limits at the 95% confidence level. These exclusion curves are seen in Figure 7.14. We are able to place lower limits at 95% confidence level on the gluino \tilde{g} mass at 2010 and 1825 GeV for the T5HH and T5ZH models, respectively. The weaker limit for the T5ZH model is due to the smaller branching fraction of the Z boson to b-quarks and our choice of signal mass window not being optimal for Z reconstruction.

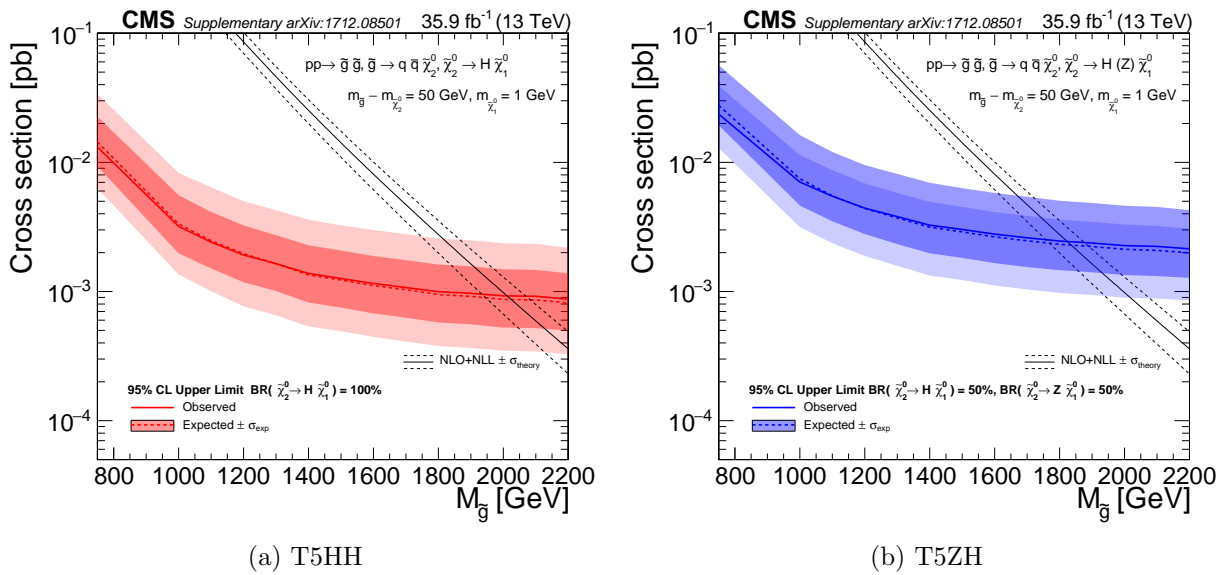


Figure 7.14: Observed and expected limits on the gluino cross section.

7.8 Reinterpretation

In Section 7.7 our results were presented in the context of limit-setting for the T5HH and T5ZH models. Many such SMS models exist within the MSSM which predict the production of

high- p_T bosons and it is therefore important to include information necessary to make predictions of yields for different final states. This is aided by providing the user with efficiencies for $b\bar{b}$ tagging and mass tagging of the AK8 jets. Tagging efficiencies for the five largest decay channels relevant to the analysis for the H boson are seen in 7.15. Tagging efficiencies for the hadronic decay modes of the Z boson are seen in Figure 7.16, the much lower mass tagging efficiency for the Z boson is due to our choice of signal mass window [85, 135 GeV] not being optimal for Z boson reconstruction. These are used to calculate the expected yields in the 6 analysis regions when performing a reinterpretation of the analysis using different final states.

For each event, the yield in each bin can be predicted by first forming the following weights using the tagging efficiencies for the leading two jets, as seen below. j_0 and j_1 represent the leading and subleading AK8 jet, respectively. The weights on the right-hand-side are p_T dependent.

- double mass tag weight = $j_{0\text{signalmass}} \cdot j_{1\text{signalmass}}$
- anti mass tag weight = $(j_{0\text{sidebandmass}} \cdot j_{1\text{signalmass}}) + (j_{1\text{signalmass}} \cdot j_{1\text{sidebandmass}}) + (j_{0\text{sidebandmass}} \cdot j_{1\text{sidebandmass}})$
- double bb tag weight = $j_{0\text{bbtag}} \cdot j_{1\text{bbtag}}$
- single bb tag weight = $(j_{0\text{bbtag}} \cdot (1 - j_{1\text{bbtag}})) + ((1 - j_{0\text{bbtag}}) \cdot j_{1\text{bbtag}})$
- anti bb tag weight = $(1 - j_{0\text{bbtag}}) \cdot (1 - j_{1\text{bbtag}})$

These weights are then combined in the following manner to determine the yields across each of the 6 bins for a single event.

- A1 weight = (single bb tag weight) · (double mass tag weight)
- A2 weight = (double bb tag weight) · (double mass tag weight)
- B1 weight = (single bb tag weight) · (anti mass tag weight)
- B2 weight = (double bb tag weight) · (anti mass tag weight)

- C weight = (anti bb tag weight) · (double mass tag weight)
- D weight = (anti bb tag weight) · (anti mass tag weight)

These weights for the 6 analysis bins (inclusive in p_T^{miss}) are then summed over all events to get the expected yields. Following this prescription, the authors performed this prediction using the T5HH model with a gluino mass of 2200 GeV and compared to the true value. The largest deficit was in the D region, with a difference of -36% difference from nominal. The greatest over-prediction is found in the B2 region, with a surplus of +8.2% events relative to nominal. The closure in the other bins fall somewhere in this range. These results are summarized in Table 7.11. As a further cross-check to the yield estimates, Table 7.12 shows the true signal event efficiencies for the T5HH model with a gluino mass of 2200 GeV.

Table 7.11: Comparison of the true reco-level event yield with those obtained via the prediction following the prescription above. The columns with the RECO or GEN labels are the prediction using RECO or GEN event variables only, respectively. The prediction was made using the T5HH MC with a gluino mass of 2200 GeV.

	RECO "truth"	RECO prediction	GEN prediction
Baseline	4.08	3.46 (-15%)	3.53 (-16%)
A1	1.21	1.18 (-2.3%)	1.26 (+3.6%)
A2	0.777	0.748 (-3.7%)	0.815 (+4.7%)
B1	0.802	0.703 (-12%)	0.664 (-21%)
B2	0.322	0.338 (+5.0%)	0.350 (+8.2%)
C	0.498	0.473 (-4.9%)	0.487 (-2.1%)
D	0.478	0.353 (25%)	0.308 (-36%)

Table 7.12: Signal efficiencies for an event to land in a given analysis bin. The efficiencies were derived using the T5HH MC with a gluino mass of 2200 GeV. Choosing a gluino mass of 1800 GeV decreases the efficiencies by a relative 5%.

	Baseline	A1	A2	B1	B2	C	D
$p_T^{\text{miss}} < 300 \text{ GeV}$	32%	9.4%	6.0%	6.2%	2.5%	3.9%	3.7%
$300 < p_T^{\text{miss}} < 500 \text{ GeV}$	2.7%	0.78%	0.52%	0.54%	0.25%	0.31%	0.30%
$500 < p_T^{\text{miss}} < 700 \text{ GeV}$	3.5%	1.0%	0.65%	0.72%	0.28%	0.43%	0.40%
$p_T^{\text{miss}} > 700 \text{ GeV}$	26%	7.6%	4.9%	5.0%	2.0%	3.1%	3.0%

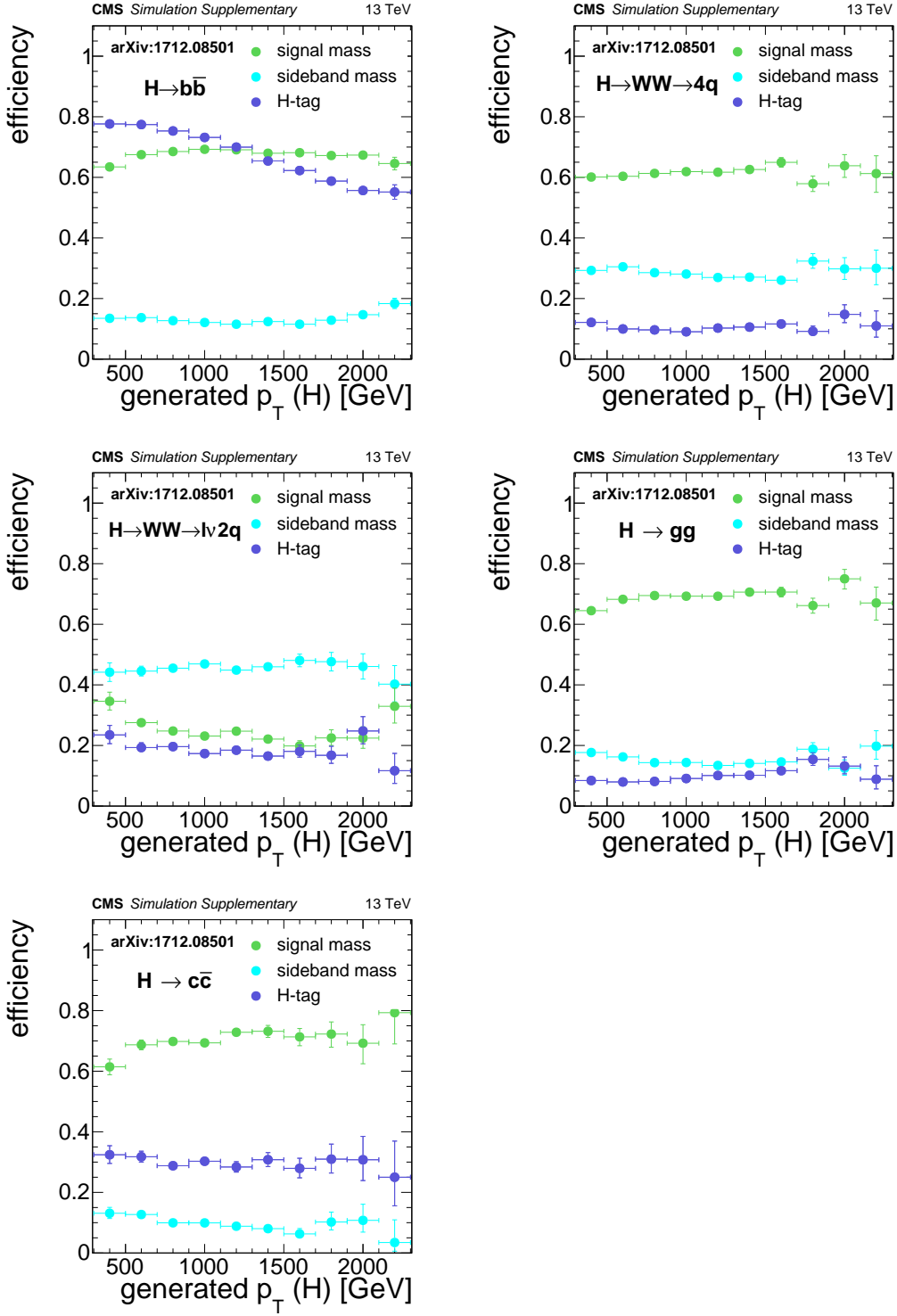


Figure 7.15: Efficiencies for an AK8 jet originating from H boson decay, relative to baseline selection. "signal mass" represents the probability the jet will have mass [85, 135 GeV]. "sideband mass" represents the probability the jet will have mass [50, 85 GeV] or [135, 250 GeV]. "H-tag" represents the probability the jet have a double-b discriminator value greater than 0.3, for jets with mass [50, 250 GeV]. Efficiencies were derived using the T5ZH MC with a gluino mass of 2200 GeV.

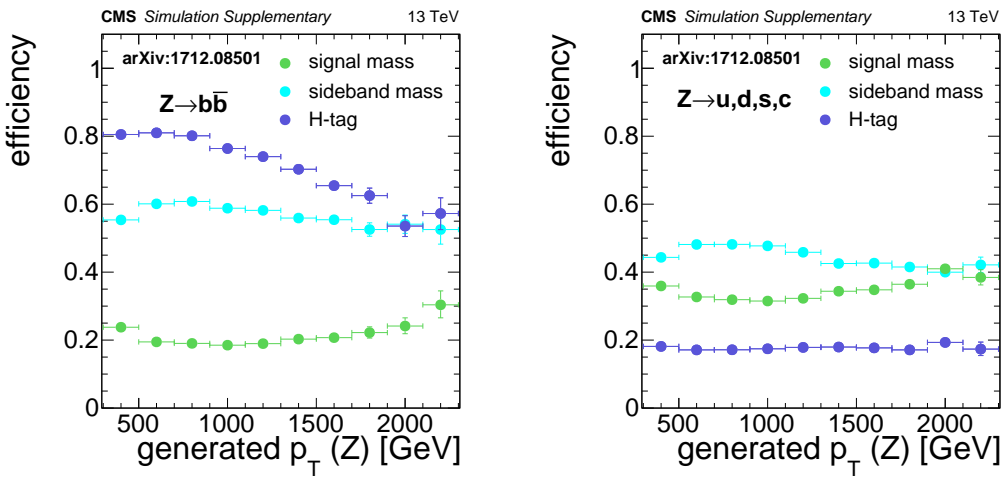


Figure 7.16: Efficiencies for an AK8 jet originating from Z boson decay, relative to baseline selection. "signal mass" represents the probability the jet will have mass [85, 135 GeV]. "sideband mass" represents the probability the jet will have mass [50, 85 GeV] or [135, 250 GeV]. "H-tag" represents the probability the jet have a double-b discriminator value greater than 0.3, for jets with mass [50, 250 GeV]. Efficiencies were derived using the T5ZH MC with a gluino mass of 2200 GeV.

Chapter 8

Conclusions

This thesis has attempted to give a broad overview of the field of high-energy and collider-based particle physics. A brief introduction to the Standard Model was given in Chapter 2. This is a quantum field theory describing the fundamental particles and gauge-mediated interactions between them which govern the matter of our Universe; these particles were summarized in Figure 2.1. In Chapter 3, we gave an overview of Supersymmetry, just one of many possible extensions to the SM which may in fact be realized in Nature. In Chapter 4 we gave a description of the Large Hadron Collider, the 27 km machine which houses a ring of two separate proton beams and provides the source of the high-energy proton-proton collisions. In Chapter 5 we gave a description of the CMS detector, an onion-like apparatus consisting of multiple layers of different particle detector technologies. Chapter 6 demonstrates how the hit information and data from the detector allows us to reconstruct the particles produced in the final states of these collisions. The SM is thus far able to provide a very good model of what we observe in these sorts of experiments.

We concluded in Chapter 7 of how an analysis of data collected by CMS is able to spot signs of physics beyond the Standard Model:

A search for physics beyond the SM was presented using events with boosted H bosons and missing transverse energy (p_T^{miss}). The search targeted events with two or more wide-angle jets (AK8) being consistent with the decay of a boosted H or Z boson decaying to $b\bar{b}$. p_T^{miss} could potentially arise in the case a supersymmetric particle escapes detection. An ABCD method uses a sideband region to predict the the SM background in our signal region. Events are categorized

according to the $b\bar{b}$ and mass tagging of the leading two AK8 jets in the event. The observed yields in the 6 signal bins are statistically compatible with the SM background expectation and no excess of events is observed. We use these results to set limits on the gluino mass for the SUSY-inspired T5HH or T5ZH models. For the T5HH model we are able to exclude gluino masses below 2010 GeV at 95% confidence level. This is with the assumption the NLSP mass is 50 GeV less than the gluino mass and that the LSP has a mass of 1 GeV. The work presented here has been published in Phys. Rev. Lett. [29].

Bibliography

- [1] CMS Collaboration, “Observation of a new boson at a mass of 125 GeV with the CMS experiment at the LHC,” *Phys. Lett. B*, vol. 716, pp. 30–61, September 2012. arXiv:1207.7235.
- [2] S. P. Martin, “A Supersymmetry Primer,” pp. 58–60, January 2016. arXiv:hep-ph/9709356.
- [3] CMS Collaboration, “The CMS Tracker Project: Technical Design Report,” 1997. CERN-LHCC-98-006 ; CMS-TDR-5.
- [4] CMS Collaboration, “The CMS Tracker Project: Addendum to the Technical Design Report,” 2000. CERN-LHCC-2000-016 ; CMS-TDR-5-add-1.
- [5] CMS Collaboration, “The CMS Electromagnetic Calorimeter Project: Technical Design Report,” 1997. CERN-LHCC-97-033 ; CMS-TDR-4.
- [6] P. Bloch, R. Brown, P. Lecoq, and H. Rykaczewski, “The CMS Electromagnetic Calorimeter Project: Addendum to the Technical Design Report,” 2002. CERN-LHCC-2002-027 ; CMS-TDR-4-add-1.
- [7] CMS Collaboration, “The CMS Hadron Calorimeter Project: Technical Design Report,” 1997. CERN-LHCC-97-031 ; CMS-TDR-2.
- [8] CMS Collaboration, “The CMS Magnet Project: Technical Design Report,” 1997. CERN-LHCC-97-010 ; CMS-TDR-1.
- [9] CMS Collaboration, “The CMS Muon Project: Technical Design Report,” 1997. CERN-LHCC-97-032 ; CMS-TDR-3.
- [10] CMS Collaboration, “Performance of the CMS Drift Tube Chambers with Cosmic Rays,” *JINST*, vol. 5, March 2010. arXiv:0911.4855.
- [11] CMS Collaboration, “Performance of the CMS cathode strip chambers with Cosmic Rays,” *JINST*, vol. 5, March 2010. arXiv:0911.4992.
- [12] CMS Collaboration, “The CMS trigger system,” *JINST*, vol. 12, p. 01020, 2017. arXiv:1609.02366.
- [13] CMS Collaboration, “Particle-flow reconstruction and global event description with the CMS detector,” *JINST*, vol. 12, p. 10003, 2017. arXiv:1706.04965.

- [14] CMS Collaboration, “Description and performance of track and primary-vertex reconstruction with the CMS tracker,” *JINST*, vol. 9, October 2014. arXiv:1405.6569.
- [15] M. Cacciari, G. P. Salam, and G. Soyez, “The anti-kt jet clustering algorithm,” *JHEP*, no. 04, p. 063, 2008. arXiv:0802.1189.
- [16] CMS Collaboration, “Identification of double-b quark jets in boosted event topologies,” 2016. CERN-LHCC-97-033 ; CMS-TDR-4.
- [17] CMS Collaboration, “Search for supersymmetry in multijet events with missing transverse momentum in proton-proton collisions at 13 TeV,” *Phys. Rev. D*, vol. 96, p. 032003, 2017. arxiv:1704.07781.
- [18] CMS Collaboration, “Search for supersymmetry in the multijet and missing transverse momentum final state in pp collisions at 13 TeV,” *Phys. Lett. B*, vol. 758, p. 152, 2016. arXiv:1602.06581.
- [19] CMS Collaboration, “Interpretation of searches for supersymmetry with simplified models,” *Phys. Rev. D*, vol. 88, p. 2017, 24 2013. arXiv:1301.2175.
- [20] CMS Collaboration, “Search for higgsino pair production in pp collisions at $\sqrt{s} = 13$ TeV in final states with large missing transverse momentum and two Higgs bosons decaying via $H \rightarrow b\bar{b}$,” *Phys. Rev. D*, vol. 97, p. 032007, 2018. arXiv:1709.04896”.
- [21] J. Alwall, R. Frederix, S. Frixione, V. Hirschi, F. Maltoni, O. Mattelaer, H.-S. Shao, T. Stelzer, P. Torrielli, and M. Zaro, “The automated computation of tree-level and next-to-leading order differential cross sections, and their matching to parton shower simulations,” *JHEP*, vol. 07, p. 079, 2014. arXiv:1405.0301.
- [22] R. D. Ball *et al.*, “Parton distributions for the LHC Run II,” *JHEP*, vol. 04, p. 040, 2015. arXiv:1410.8849.
- [23] T. Sjstrand, S. Ask, J. R. Christiansen, R. Corke, N. Desai, P. Ilten, S. Mrenna, S. Prestel, C. O. Rasmussen, and P. Z. Skands, “An introduction to PYTHIA 8.2,” *Computer Physics Communications*, vol. 191, pp. 159–177, June 2015. arXiv:1410.3012.
- [24] S. Agostinelli *et al.*, “GEANT4—a simulation toolkit,” *Nucl. Instrum. Meth. A*, vol. 506, p. 250, July 2003. [https://doi.org/10.1016/S0168-9002\(03\)01368-8](https://doi.org/10.1016/S0168-9002(03)01368-8).
- [25] CMS Collaboration, “Search for supersymmetry in multijet events with missing transverse momentum in proton-proton collisions at 13 TeV,” CMS AN-16-350.
- [26] M. Cacciari, S. Frixione, M. L. Mangano, P. Nason, and G. Ridolfi, “The $t\bar{t}$ cross-section at 1.8 TeV and 1.96 TeV: A Study of the systematics due to parton densities and scale dependence,” *JHEP*, vol. 4, no. 2004, p. 068, 2004. arXiv:hep-ph/0303085.
- [27] S. Catani, D. de Florian, M. Grazzini, and P. Nason, “Soft gluon resummation for Higgs boson production at hadron colliders,” *JHEP*, vol. 07, p. 028, 2003. arXiv:hep-ph/0306211.
- [28] I. Belotelov, I. Golutvin, D. Bourilkov, A. Lanyov, E. Rogalev, M. Savina, and S. Shmatov, “Identification and calibration of boosted hadronic W/Z bosons at 13 TeV,” CMS AN-16-215.

- [29] CMS Collaboration, “Search for physics beyond the standard model in events with high-momentum Higgs bosons and missing transverse momentum in proton-proton collisions at 13 TeV,” *Phys. Rev. Lett.*, vol. 120, p. 241801, 2018. arXiv:1712.08501.